Flow physics and RANS modelling of oblique shock/turbulent boundary layer interaction

Brandon Morgan†, K. Duraisamy, N. Nguyen, S. Kawai‡ and S. K. Lele

Department of Aeronautics and Astronautics, Stanford University, Stanford, CA 94305, USA

Large-eddy simulation (LES) is utilized to investigate flow physics and lower-fidelity modelling assumptions in the simulation of an oblique shock impinging on a supersonic turbulent boundary layer (OSTBLI). A database of LES solutions is presented, covering a range of shock strengths and Reynolds numbers, that is utilized as a *surrogate-truth model* to explore three topics. First, detailed conservation budgets are extracted within the framework of parametric investigation to identify trends that might be used to mitigate statistical (aleatory) uncertainties in inflow conditions. It is found, for instance, that an increase in Reynolds number does not significantly affect length of separation. Additionally, it is found that variation in the shock-generating wedge angle has the effect of increasing the intensity of low-frequency oscillations and moving these motions towards longer time scales, even when scaled by interaction length. Next, utilizing the LES database, a detailed analysis is performed of several existing models describing the low-frequency unsteady motion of the OSTBLI system. Most significantly, it is observed that the length scale of streamwise coherent structures appears to be dependent on Reynolds number, and at the Reynolds number of the present simulations, these structures do not exist on time scales long enough to be the primary cause of low-frequency unsteadiness. Finally, modelling errors associated with turbulence closures using eddy-viscosity and stress-transport-based Reynolds-averaged Navier–Stokes (RANS) simulations are investigated. It is found that while the stress-transport models offer improved predictions, inadequacies in modelling the turbulence transport terms and the isotropic treatment of the dissipation is seen to limit their accuracy.

Key words: turbulence modelling, turbulence simulation, wave–turbulence interactions

1. Introduction

Although the first measurements of shock-induced separation were made as early as the late 1930s (Ferri 1940), there is still much about the physical dynamics of shock/turbulent boundary layer interaction (STBLI) which remains unclear. It has been shown, for instance, that fully separated STBLIs experience a low-frequency oscillation of the shock structure and a periodic expansion/contraction of

† Current affiliation: Lawrence Livermore National Laboratory, USA. Email address for correspondence: bmorgan1@stanford.edu

‡ Current affiliation: Institute of Space and Astronautical Science, JAXA, Japan
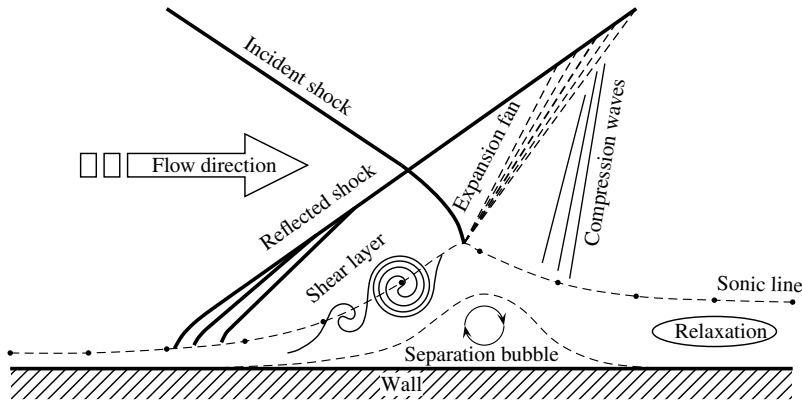
FIGURE 1. Illustration of a typical oblique shock/boundary layer interaction (Touber & Sandham 2008).

the separation bubble (Dolling & Murphy 1983). Despite a number of experimental and numerical studies on the nature of this low-frequency unsteadiness, there remains dissidence within the community as to the precise mechanism responsible. Furthermore, it is generally accepted that traditional eddy-viscosity-based Reynolds-averaged Navier–Stokes (RANS) simulations may provide unsatisfactory prediction of mean pressure, skin friction, and heat transfer in all but the weakest of interactions (Knight & Degrez 1998). Of course, the existence of low-frequency unsteadiness as a dominant flow feature may contribute to inaccuracies in steady RANS solutions; however, it has been suggested that more fundamental issues such as the use of a single length scale or the application of wall functions in eddy viscosity models may contribute to their inaccuracy in simulations of separated flows (Dolling 2001). It is therefore the objective of the present work to explore the physics of oblique STBLI with high-fidelity large-eddy simulation (LES) over a range of incident shock strengths and Reynolds numbers in order to: (i) identify important trends with respect to the flow conditions which may, in general, be uncertain; (ii) investigate potential mechanisms for low-frequency unsteadiness; and (iii) address potential causes of failure in lower-fidelity RANS models.

STBLIs occur in a number of practical and experimental configurations, including compression corner, expansion-compression corner, double fin, normal shock impingement, and oblique shock impingement configurations (Knight *et al.* 2002). The present study focuses on the unit problem of an oblique shock wave impinging on a turbulent boundary layer (OSTBLI), illustrated schematically in figure 1. The incident shock impinges on a turbulent boundary layer that is developing over a flat plate. The adverse pressure gradient due to the shock causes a region of separated flow to form in the boundary layer, and compression waves off the leading edge of this bubble coalesce to form the reflected shock. On the reverse side of the separated region, a Prandtl–Meyer expansion fan develops and joins the reflected shock structure. In addition, the separation bubble undergoes a low-frequency expansion/contraction, which perhaps causes (or alternately is a result of) a low-frequency motion in the reflected shock structure.

The cause of this low-frequency unsteadiness remains an open issue, and several explanations have been proposed. Ganapathisubramani, Clemens & Dolling (2009)

have proposed that long vortical superstructures of the order of 50 boundary layer thicknesses exist in the turbulent boundary layer and that the interaction of these structures with the shock could be the cause of unsteadiness. An acoustic feedback mechanism has been proposed by Pirozzoli & Grasso (2006) in which acoustic waves propagate upstream from the tip of the incident shock, are amplified, and create a resonance which is suggested as responsible for the low-frequency unsteadiness. Piponniau *et al.* (2009) have proposed a model for low-frequency unsteadiness based on the mass budget of a separation bubble requiring periodic entrainment and release of mass at a long time scale. Robinet (2007) has investigated the linear stability of STBLI in the context of laminar interactions and found evidence of a global mode unsteadiness for sufficiently wide domains and large shock angles, which can be linked to the size of the separation bubble. Although based on a less rigorous multi-time scale-decomposition argument, Touber & Sandham (2009*b*) have also observed similar global-mode instability using a mean flow field derived from turbulent LES of STBLI. Most recently, Touber & Sandham (2011) have derived a first-order stochastic model of OSTBLI dynamics, which is shown to respond to white noise with a low-frequency response. This analysis is further supported by experimental observations by Poggie & Smits (2005), which revealed that shock position fluctuations in several blunt fin flows could be modelled accurately by linearly damped Brownian motion, consistent with the model first described by Plotkin (1975). In the Plotkin model, shock displacement is postulated to be limited by an unspecified linear restoring mechanism, such that the shock position could be modelled according to a first-order ordinary differential equation (ODE). Despite the range of possible mechanisms, however, most experiments and simulations agree that the unsteadiness occurs at time scales between 10 and 100 times the characteristic time scale of the incoming boundary layer, δ/u_∞, defined based on the undisturbed boundary layer velocity thickness, δ, and the mean free stream velocity, u_∞.

Early experimental work on STBLI has largely focused on the compression ramp geometry; however, a number of high-quality experiments have recently been carried out to investigate OSTBLI by groups at Princeton University (Bookey, Wyckham & Smits 2005*a*; Bookey *et al.* 2005*b*), the Delft University of Technology (TUD) (Humble, Scarano & van Oudheusden 2007; Humble *et al.* 2009*a*,*b*), the University of Michigan (Lapsa & Dahm 2010), and Institut Universitaire des Systèmes Thermiques Industriels (IUSTI) in Marseille, France (Dupont, Haddad & Debieve 2006; Dussauge, Dupont & Debieve 2006; Debieve & Dupont 2009; Delery & Dussauge 2009). In the present study we focus on the IUSTI experiments, which were performed at a more accessible Reynolds number than the TUD experiments. Additionally, these experiments have been explored by a number of previous computational studies, which provide a convenient basis for comparison to establish confidence in solution quality. Touber & Sandham (2009*b*) and Hadjadj *et al.* (2010) have previously performed LES computations of the IUSTI experiment near the experimental Reynolds number ($Re_\theta = 5100$, based on the momentum thickness, θ), and Pirozzoli & Bernardini (2011) have recently completed a direct numerical simulation (DNS) of the same flow conditions, at a reduced Reynolds number of $Re_\theta = 2300$. In general, most previous computational studies have focused on a single set of flow conditions, and there are only a limited number of studies that consider the effects of parametric variation. Touber & Sandham (2009*a*) did perform a study that compared three different large-eddy simulations of OSTBLI corresponding to three different experimental conditions at varying Mach number, wedge (shock generator) angle, and Reynolds number. They found, for instance, that the interaction length is proportional to the impinging shock

strength when scaled by incoming boundary layer thickness and wall-shear stress. However, since these simulations varied all three variables simultaneously, it is difficult to draw conclusions regarding the effect of any single variable on OSTBLI physics. Pirozzoli *et al.* (2010) have additionally performed limited parametric variation with LES, studying variation with respect to four wedge angles at constant Reynolds number.

In the present study, we present results from an extensive database of LES results, spanning a total of 19 cases with varying grid resolution, domain size, Reynolds number, and wedge angle. Work is focused on extracting from this database trends and diagnostic data that might be useful in identifying or quantifying uncertainties in RANS simulations of OSTBLI. In §2, a brief discussion of the mathematical formulation is presented, including numerical schemes and flow conditions used in the present study. In §2.3, the cause and effect of numerical dissipation in the present high-fidelity numerics is investigated in some detail, and in §2.4, a baseline simulation is validated through a grid resolution study and through comparisons with DNS and experimental data. Then, in §3, results from the present investigation are presented. First, in §3.1, trends are investigated in mean flow variables such as skin friction and wall pressure, intensity and time scale of low-frequency motion, and the balance of turbulence kinetic energy (TKE) with respect to variation in wedge angle (shock strength) and Reynolds number. Next, in §3.2, an assessment is made of the evidence for and against several popular mechanisms proposed to explain the low-frequency unsteady motion of the interaction. To support this analysis, a time history is extracted from the present database of the integrated conservation equations applied to moving control volumes representing the separation bubble and the greater interaction region. Then, in §3.3, results are compared with RANS simulations utilizing a standard two-equation model and a full Reynolds stress transport model. Through analysis of TKE and Reynolds stress transport budgets, weaknesses in existing model formulations are identified. Finally, in §4, conclusions are drawn, and recommendations are made concerning the direction of future work.

2. Computational setup and validation

2.1. *Mathematical models*

The LES code used in the present study solves the spatially filtered compressible Navier–Stokes equations for an ideal non-reactive gas. A sixth-order compact difference scheme (Lele 1992) is used to solve the governing equations in transformed curvilinear coordinates, and Gauss–Seidel alternate directional implicit factorization (Obayashi, Fuji & Gavali 1988; Iizuka 2006) is used with three Newton–Raphson sub-iterations for time integration with second-order backwards differencing. At each time step, an eighth-order low-pass spatial filtering scheme (Lele 1992) (with filtering parameter $\alpha_f = 0.495$) is applied once to the conservative variables to ensure stability, and we utilize second- and fourth-order near-boundary formulas developed by Gaitonde & Visbal (1998) that retain the tridiagonal form of the equation set. In order to maintain time accuracy of the solution, the time step is selected such that the Courant–Friedrichs–Lewy (CFL) number is near, but less than, unity. This choice of time-integration scheme and time step size has been used previously by Kawai, Shankar & Lele (2010) and was shown to be sufficiently accurate for the simulation of compressible turbulence.

Since central differencing schemes, such as the compact differencing scheme used in the present study, can generate non-physical oscillations in regions of high

gradient, a shock-capturing scheme is desirable; however, such a scheme must not be so dissipative that it eliminates smaller scales of turbulence. For this reason, the localized artificial diffusivity (LAD) method of shock-capturing (Kawai *et al.* 2010) is applied. This method, which is based on Cook's method (Cook 2007) of adding artificial coefficients to the fluid transport terms (improved by modification of Mani, Larsson & Moin (2009) and extended for use with curvilinear meshes by Kawai & Lele (2008)), is enhanced by the addition of a dilatation-based switching function (shock sensor) in the formulation of the artificial bulk viscosity. This switching function removes unnecessary bulk viscosity within expansion and shock-free weakly compressible turbulence regions and allows it to take effect only near shocks. Aside from the implicit model created by addition of the artificial bulk viscosity and thermal conductivity, no additional SGS model is used. Detailed description of the governing equations and the LAD scheme can be found in previous works (Kawai & Lele 2008, 2010; Kawai *et al.* 2010). Indeed, there are many ways to approach the problem of modelling the subgrid scales, and an implicit approach such as that used in the present study is not without its limitations. For this reason, we do not presume to promote the use of implicit LES in the general sense. However, as Kawai *et al.* (2010) have shown, when the high-order numerics used in the present study are applied with sufficiently high grid resolution, the implicit approach actually out-performs a traditional LES approach using an explicit SGS model. Specifically, it was found that use of an explicit SGS model resulted in additional damping of the resolved turbulence at similar Reynolds number and grid resolution. By conducting a grid resolution study and by computing TKE dissipation introduced by our numerics, we are able to establish that our simulations are conducted under the necessary resolution required to use an implicit approach in an appropriate manner.

The RANS code used in this study is the second-order accurate, unstructured 'Joe' code developed at Stanford University. This code solves the compressible Reynolds-averaged Navier–Stokes equations on unstructured meshes of arbitrary polyhedral elements using a finite volume approach with implicit time marching. Further details on the formulation of the Joe RANS/URANS code may be found in the work by Pecnik *et al.* (2009).

2.2. *LES database*

The LES database utilized in the present study consists of 19 total simulations of oblique STBLI over an adiabatic flat plate with free stream Mach number $M_\infty = 2.28$ and varying grid resolutions, domain sizes, Reynolds numbers, and wedge angles, ϕ. In all simulations, periodic boundary conditions are applied in the spanwise direction, and recycling/rescaling with dynamic reflection (RR + DR) (Morgan *et al.* 2011*b*) is used to generate inflow turbulence. RR + DR represents an improvement of the traditional recycling/rescaling (RR) method for compressible boundary layers developed by Urbin & Knight (2001) in which the recycled profile is first reflected about a dynamically selected spanwise location. This method has been shown to eliminate spurious spatiotemporal correlations associated with the recycling frequency without damaging the physical structure of the turbulence, as illustrated in figure 2. This figure (reproduced from Morgan *et al.* 2011*b*) plots contours of spatiotemporal covariance of streamwise velocity in Mach 2.28 boundary layers simulated using standard RR and with the improved RR + DR method. In both simulations, a flow-through time (FTT) indicates the non-dimensional time required for the potential flow to traverse from the inlet plane to the recycling capture plane (∼12 boundary layer thicknesses, δ_0). While the leftmost band of contours in the plots in figure 2
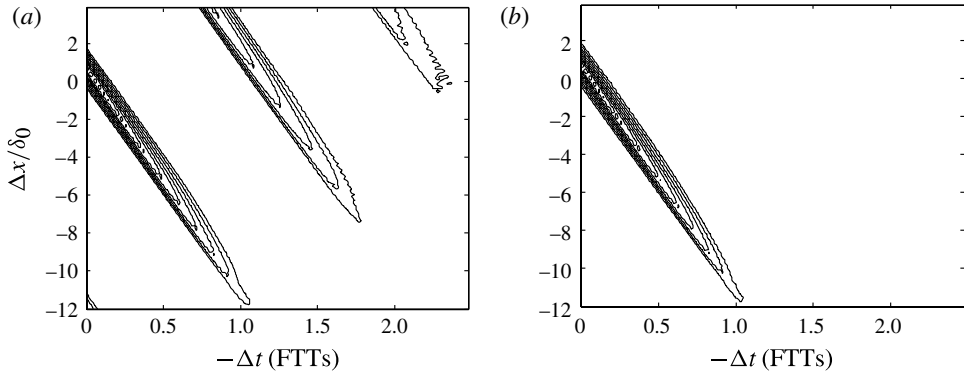
FIGURE 2. Ten logarithmically spaced contours of streamwise velocity spatiotemporal covariance function, $Cov(u(x, t), u(x + \Delta x, t + \Delta t))$, between 0.1 and 1.0 at $y/\delta_0 = 0.7$. (*a*) Correlation with standard RR; (*b*) correlation with improved RR + DR.

is physical and associated with the natural convection of turbulent structures, the repeated bands that are observed using standard RR are a product of the periodic re-introduction of self-similar eddies. With RR + DR, however, spanwise 'scrambling' is utilized to eliminate these non-physical correlations; a full discussion of the formulation and effect of the RR + DR procedure is given by Morgan *et al.* (2011*b*).

Our approach to studying OSTBLI is to simulate an undisturbed turbulent boundary layer simultaneously and in a separate mesh from the interaction. The recycled profile is then extracted and imposed as inflow conditions to the interaction mesh. For this reason, the upstream boundary layer thickness δ_0 is evaluated at the inlet of the interaction mesh (and is equivalent to the capture plane in the undisturbed boundary layer simulation). The far-field boundary opposite the adiabatic wall is a buffer region and is sufficiently high that all disturbances exit through a simple extrapolation outflow. In the interaction mesh, above the incoming boundary layer, Rankine–Hugoniot relations are used to specify free stream values before and after the shock at the inlet plane. In the case of wedge angle variations, the height of the shock on the inlet plane is varied such that the inviscid shock impingement point (that is, the point at which the oblique shock would impinge on the flat plate in the absence of a boundary layer), x_0, is held constant.

Figure 3 summarizes the various simulations undertaken and establishes the notation used to refer to simulations in the remainder of this study. Note that the values in figure 3 are *a priori* estimations; due to variations in incoming boundary layer properties, resolutions and Reynolds numbers vary slightly from these values. Tables 3 and 4 in the Appendix provide detailed flow conditions and grid data, respectively, for each of the 19 simulations computed. Flow conditions are chosen to be generally comparable to DNS by Pirozzoli & Bernardini (2011) ($M_\infty = 2.28$, $Re_\theta = 2300$, $\phi = 8°$) and experiment by Piponniau *et al.* (2009) ($M_\infty = 2.28$, $Re_\theta = 5100$, $\phi = 7$–$9.5°$). The ratio of effective mesh spacing $\Delta = (\Delta x \, \Delta y \, \Delta z)^{1/3}$ to the local Kolmogorov length scale in DNS results by Pirozzoli & Bernardini (2011) is reported to be less than 5 throughout the interaction. At L4 resolution, the present LES results are comparable to DNS grid spacing in the wall-normal dimension; although they are coarser by an approximate factor of two in the spanwise and streamwise dimensions.

Refinement level	Δx^+	Δy^+	Δz^+
L1	50–30–50	1–30	30
L2	30–17–30	1–15	15
L3	25–14–25	1–12.5	12.5
L4	20–11–20	1–10	10

$$Re_\theta = \{1500, 2300, 4800\}$$

Grid type	L_x	L_y	L_z
STD	$10\delta_0$	$8.5\delta_0$	$3.0\delta_0$
WIDE	$10\delta_0$	$8.5\delta_0$	$6.0\delta_0$
LONG	$20\delta_0$	$12.5\delta_0$	$3.0\delta_0$

Wedge angle = $\{6.5, 7.0, 7.5, 8.0, 8.5, 9.0, 9.5\}$

How to read a descriptor string:

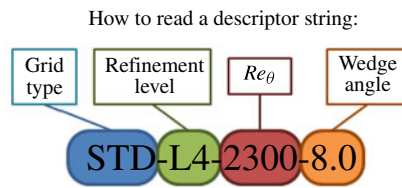| Grid type	Refinement level	Re_θ	Wedge angle

STD-L4-2300-8.0

FIGURE 3. (Colour online) A colour-coded key to summarize simulation flow conditions and naming conventions. Grid dimensions given are for the interaction mesh only, and regions of stretching are indicated by a dash. Descriptor strings are used to refer to individual simulations without ambiguity. L_x, L_y and L_z refer to the computational domain extent in the streamwise, wall-normal, and spanwise directions, respectively, in terms of upstream boundary layer thicknesses (δ_0). Δ^+ denotes grid spacings in wall units.

2.3. *Numerical dissipation*

As described previously, the numerical code used in the present study employs an eighth-order, spatial filtering scheme (Lele 1992) (with filtering parameter $\alpha_f = 0.495$) once per time step to ensure stability. Unless the spatial resolution is very high, the effect of this filtering can be to dissipate turbulence kinetic energy (TKE), which may adversely impact the resolved TKE budget. Fortunately, it is possible to quantify the numerical dissipation due to filtering by computing TKE before and after the filtering step. In this section, we investigate the role that numerical dissipation may play by considering the TKE budget for an undisturbed turbulent boundary layer at differing levels of grid resolution. Each simulation in this section is performed with $M_\infty = 2.28$, $Re_\theta = 2300$, and a non-dimensional time step of $\Delta(tu_\infty/\delta_0) = 0.0006$ (CFL ≈ 0.5). The transport equation for TKE ($k = \widetilde{u_i'' u_i''}/2$) is given in compressible form as follows (Pirozzoli, Grasso & Gatski 2004):

$$\frac{\partial \overline{\rho} k}{\partial t} = C_k + T_k + P_k + V_k + K_k + D_k. \tag{2.1}$$

In the above equation, C_k, T_k, P_k, V_k, D_k and K_k represent, respectively, terms due to convection, turbulent transport, production, viscous diffusion, dissipation, and compressibility effects. Explicitly, these terms are given by

$$C_k = -\frac{\partial \overline{\rho} \widetilde{u}_j k}{\partial x_j}, \quad P_k = -\overline{\rho \widetilde{u_i'' u_j''}} \frac{\partial \widetilde{u}_i}{\partial x_j}, \quad V_k = \frac{\partial}{\partial x_j}\left(\overline{\sigma_{ij}' u_i''}\right), \tag{2.2}$$

$$T_k = -\frac{\partial}{\partial x_j}\left[\frac{1}{2}\overline{\rho \widetilde{u_i'' u_i'' u_j''}} + \overline{p' u_j''}\right], \quad K_k = \overline{p' \frac{\partial u_i''}{\partial x_i}} + \overline{u_i''\left(\frac{\partial \overline{\sigma}_{ij}}{\partial x_j} - \frac{\partial \overline{p}}{\partial x_i}\right)}, \tag{2.3}$$
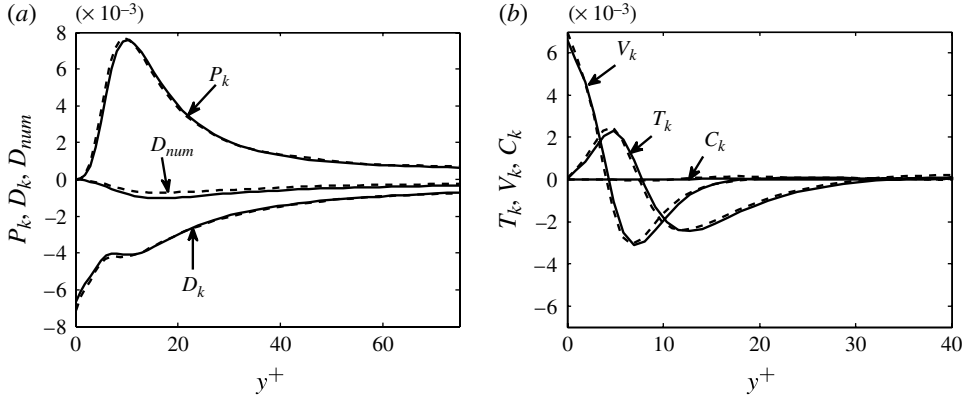
FIGURE 4. Effect of grid resolution on TKE budget in undisturbed boundary layer. Normalization by free stream density, free stream velocity, and local boundary layer thickness. Solid lines, STD-L2-2300-8.0; dashed lines, STD-L4-2300-8.0.

$$D_k = D_{res} + D_{num} = \left[-\overline{\sigma'_{ij} \frac{\partial u''_i}{\partial x_j}} \right] - \left[\frac{\rho_\infty}{\Delta \tau} \left(\widehat{\widetilde{k}} - k \right) \right]. \qquad (2.4)$$

In these equations, ρ indicates density, t indicates time, x_j indicates spatial dimension, u_j indicates the velocity vector, p indicates pressure, and σ_{ij} indicates the viscous stress tensor. An overbar is used to denote Reynolds averaging, a tilde denotes Favre averaging, and a circumflex denotes a quantity computed on the filtered field.

Note that total dissipation, D_k, is defined as the sum of the resolved dissipation, D_{res}, and the numerical dissipation, D_{num}. In this case, it is assumed that the most significant contribution to numerical dissipation is the spatial filtering. To assess the effect of numerical dissipation on the budget, figure 4 plots the TKE budget terms for two levels of grid resolution (L2 and L4). While it is clear that increasing the grid resolution decreases the peak $|D_{num}|$, total dissipation and production do not seem to be significantly changed. There may be some effect on the peak turbulent transport very near the wall; however, beyond $y^+ \approx 25$, there appears to be no difference between the two levels of refinement. Therefore, we conclude that grid resolution levels L2 and above are sufficient to appropriately resolve TKE production, with numerical dissipation due to filtering effectively acting as a subgrid model of dissipation at unresolved scales. Note that values of K_k are not plotted in figure 4 because they are essentially negligible. Expanded discussion of the role of numerical dissipation in the present numerics is given by Morgan (2012).

2.4. *Baseline validation*

2.4.1. *Effect of grid resolution and domain size*

Before examining trends with respect to Reynolds number and wedge angle, it is important to establish confidence in the quality of the baseline solution; this is the motivating factor behind the grid resolution and domain sizing studies. It is desirable to establish that the relevant scales of turbulence are accurately captured and that the solution is not unduly influenced by the computational domain. Touber & Sandham (2009b), for instance, have found that a domain which is not sufficiently wide in the spanwise direction may result in a non-physical increase in the size of the computed separation bubble. Table 3 in the Appendix tabulates characteristic
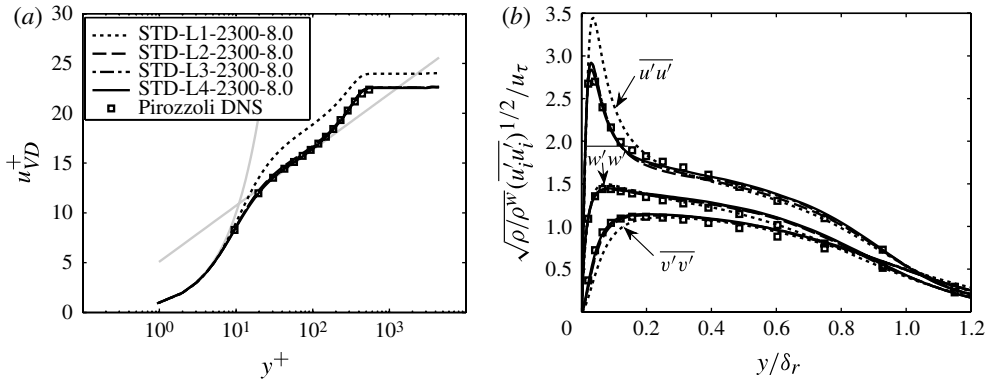
FIGURE 5. Undisturbed incoming boundary layer: (*a*) van-Driest-transformed mean streamwise velocity and (*b*) r.m.s. velocity fluctuations. Top curve, streamwise velocity components; middle curve, spanwise; bottom curve, wall-normal.

quantities and compares them with DNS (Pirozzoli & Bernardini 2011) and experiment (Piponniau *et al.* 2009). It is clear that for levels of refinement L2–L4, the agreement is quite good in sensitive quantities such as skin friction and friction velocity (taking into account slight discrepancies in Re_θ), although the present simulation consistently predicts a shape factor H that is lower than the DNS. Figure 5 compares mean velocity and r.m.s. velocity fluctuation profiles for the four levels of refinement at the same flow conditions as the DNS. In figure 5(*a*), we plot for reference a linear relationship (in grey) in the viscous sublayer and a logarithmic relationship (with von Kármán constant $\kappa = 0.41$ and log-law constant $C = 5.1$) in the logarithmic region. With the exception of the L1 simulation, which is clearly under-resolved, good agreement is observed with both theory and DNS in mean profile. In figure 5(*b*), it is again observed that while the L1 simulation is too coarse, there is good agreement with DNS for all other levels of grid resolution.

As discussed in §2.1, recycling/rescaling with a development length of $12\delta_0$ is utilized based on the results of Morgan *et al.* (2011*b*). To investigate any potential upstream influences in pressure, figure 6 illustrates r.m.s. wall pressure as well as instantaneous wall pressure fluctuations in the boundary layer profile which is introduced to the inlet of the STD-L2-2300-8.0 interaction simulation at $(x - x_0)/\delta_0 \approx -5.7$. The r.m.s. pressure curve appears to have levelled off well upstream of the extraction plane, and the r.m.s. value of approximately 3% of the free stream is in good agreement with values reported by Pirozzoli & Bernardini (2011) as well as with the level of fluctuations observed in the instantaneous pressure plot.

Figure 7 furthermore compares contributions to the TKE budget in the undisturbed boundary layer with DNS results by Pirozzoli & Bernardini (2011). The comparison DNS results were obtained using a hybrid central-differencing/fifth-order-weighted essentially non-oscillatory (WENO) discretization with switching controlled by a modified Ducros sensor. Although the present work is slightly more resolved in the outer boundary layer wall-normal direction, the comparison DNS has finer resolution in the spanwise and streamwise dimensions by approximately a factor of two over the L4 grid resolution. Additionally, the DNS numerics do not utilize artificial dissipation or spatial filtering, making the results by Pirozzoli & Bernardini (2011) the highest-
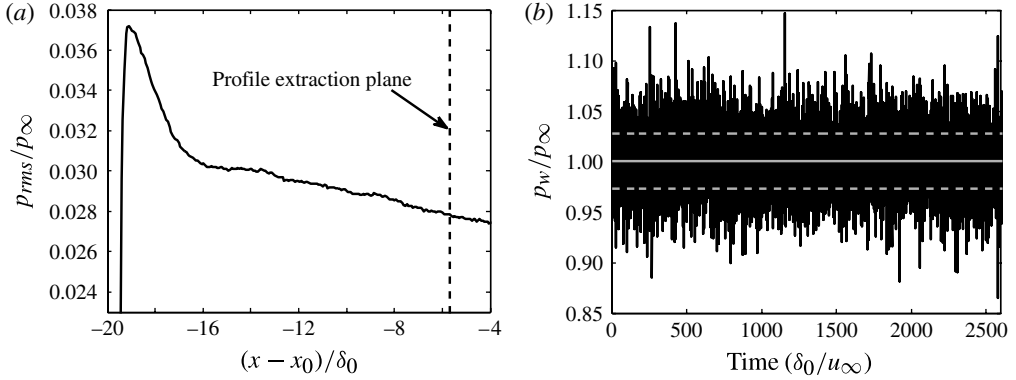
FIGURE 6. Pressure fluctuations in the undisturbed boundary layer from the STD-L2-2300-8.0 simulation: (*a*) spatially varying r.m.s. wall pressure, and (*b*) instantaneous wall pressure at the profile extraction plane as a function of time. Solid grey line, mean ($\mu_p = 1.0001$); dashed grey lines, one standard deviation ($\sigma_p = 0.027418$).
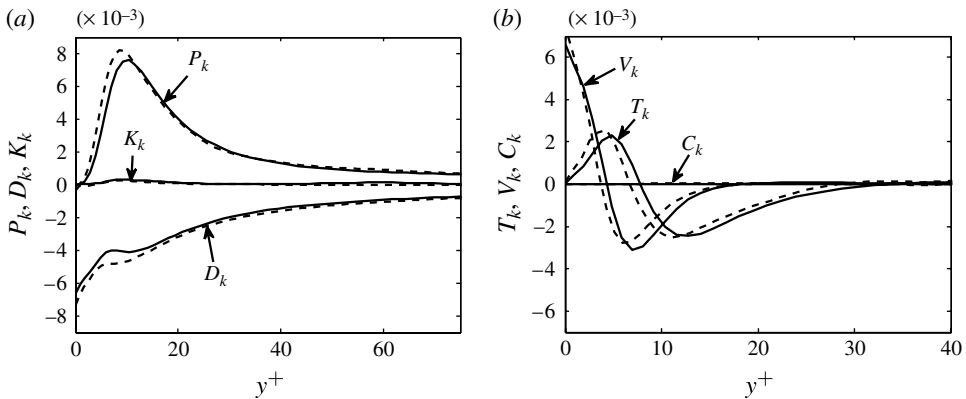

FIGURE 7. Comparison of baseline (STD-L2-2300-8.0) TKE budget with DNS by Pirozzoli & Bernardini (2011) at $(x - x_0)/\delta_0 = -5.58$. Normalization by free stream density, free stream velocity, and local boundary layer thickness. Solid lines, present LES; dashed lines, Pirozzoli DNS.

fidelity simulation data of the IUSTI experiments available to the authors and therefore a reasonable baseline for validation of our own data. While there are some minor discrepancies in the location and magnitude of peak quantities, the budgets generally agree quite well, and recalling figure 4, we consider our statistics to be nearly grid converged.

In figure 8, solution quality is investigated in the interaction. Figure 8(*a*) plots coefficient of skin friction across the interaction, and figure 8(*b*) plots wall pressure. These figures highlight how grid resolution can affect the size and location of the predicted separation bubble. In particular, it is clear that the under-resolved simulation at grid level L1 predicts separation further downstream, with higher peak skin friction in the separation bubble. While the L4 simulation agrees quite well with the DNS, the L2 and L3 simulations seem to slightly under-predict the size of the separation bubble
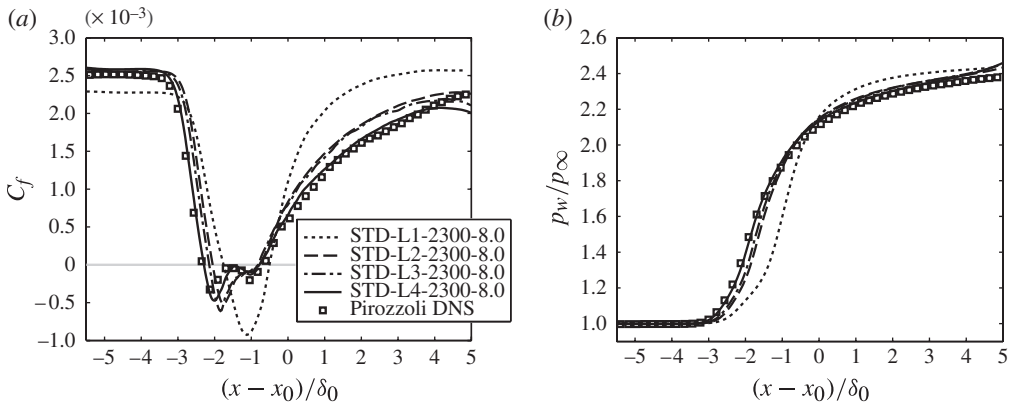
FIGURE 8. Effect of grid resolution on separation bubble: (*a*) skin friction coefficient, and (*b*) wall pressure.

and do not appear to capture the complex double-peak behaviour of the skin friction curve in the separated region. As a result, in figure 8, the pressure rise and recovery characteristics differ somewhat from the DNS (although the difference in pressure recovery may also be related to the previously reported discrepancy in undisturbed boundary layer shape factor).

It has been shown previously that domain size can affect the size of the separation bubble (Touber & Sandham 2009*b*). Usually, this occurs when the domain is not wide enough in the spanwise dimension such that turbulent structures are not de-correlated and may mimic the effect of spanwise confinement on the separation bubble (Garnier 2009). Of course, a domain which is not long enough in the streamwise direction might also affect the pressure recovery and, as a result, the size of the separation bubble. Indeed, the outflow boundary condition is merely first-order extrapolation on all variables. It is therefore expected that some disturbance should be observed in the subsonic boundary layer flow at the outlet (e.g. skin friction and wall pressure behaviour around $(x - x_0)/\delta_0 \approx 5.0$ in figure 8). To determine the effect, if any, that domain size has on our solution, we have computed interactions at L2 resolution using domains with double spanwise (WIDE) and double streamwise (LONG) dimensions. Figure 9 plots time-averaged skin friction and wall pressure calculated with these domains. Two interesting observations may be made from figure 9; first, it is observed over the region $(x - x_0)/\delta_0 = -5$ to 5 (the domain of the STD mesh) that there is virtually no difference in the computed skin friction or wall pressure. Secondly, in the LONG simulation, the pressure is seen to recover the same outlet value predicted by the DNS. In the case of the extended streamwise domain, streamwise gradients are less extreme at the outlet; thus, it is expected that the effect of disturbances at the outlet should be less severe. The key point to take away from comparison with the LONG mesh is, therefore, not that an extended domain reduces the disturbance at the outlet. Rather, the key point is that the physics in the region of interest – the interaction region – are unaffected by the presence of the disturbance, which is admittedly present at the outlet of the STD domain.

Figure 10 further investigates the effect of domain size on solution quality by looking at two-point velocity correlations from the STD-L2-2300-8.0 simulation. In figure 10(*a*), contours of the two-point streamwise velocity correlation function C_{uu} are
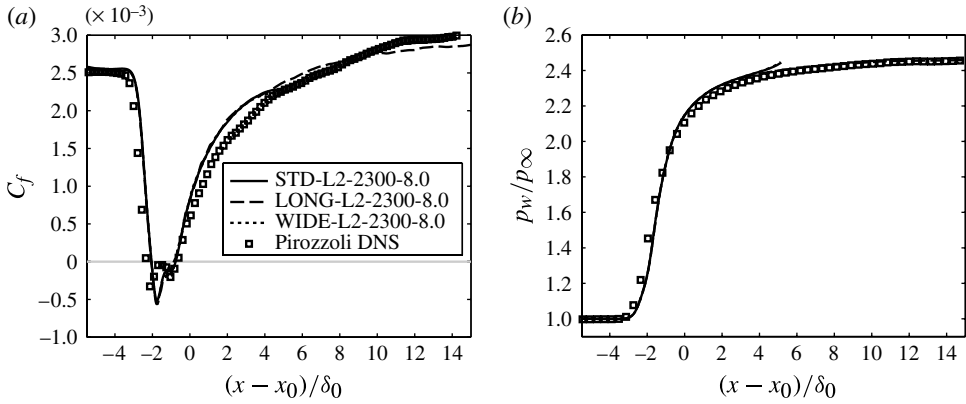
FIGURE 9. Effect of domain size on separation bubble: (*a*) skin friction coefficient, and (*b*) wall pressure.
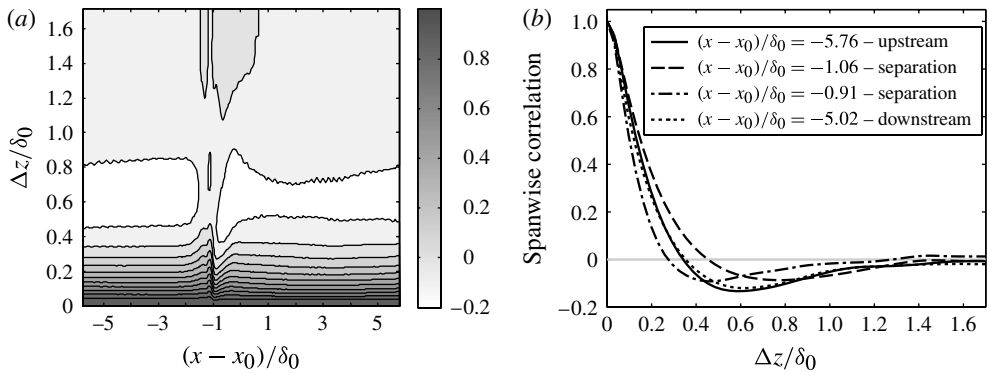

FIGURE 10. Two-point streamwise velocity correlations in the spanwise direction from baseline (STD-L2-2300-8.0): (*a*) contours of C_{uu} plotted against streamwise location and spanwise distance at $y/\delta_0 = 0.7$; (*b*) C_{uu} plotted at several streamwise locations.

plotted against streamwise location and spanwise distance at a height of $0.7\delta_0$ above the wall, where

$$C_{uu}(x, y, \Delta z) = \overline{u'(x, y, z)u'(x, y, z + \Delta z)}/u(x, y)_{rms}^2. \qquad (2.5)$$

It is clear that the integral length scale in the interaction region increases then decreases sharply when compared with the length scale of the incoming boundary layer. In figure 10(*b*), however, by plotting the correlations at several streamwise stations, it is seen that although the integral length scale changes in the separation bubble, the flow is apparently de-correlated before a distance equal to half the span. This reinforces the conclusion drawn from figure 9 that the spanwise domain size is sufficient with the STD meshes. It is also interesting to note that the sharp decrease in integral length scale occurring around $(x - x_0)/\delta_0 = -0.9$ corresponds to the second streamwise skin friction peak observed in figures 8 and 9. This suggests that the shock wave may be acting as a low-pass filter on larger energetic structures (damping smaller,
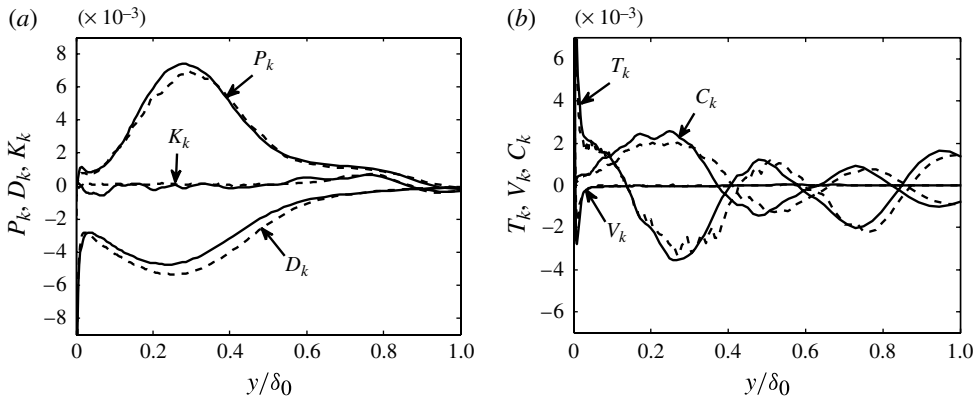
FIGURE 11. Comparison of baseline (STD-L2-2300-8.0) TKE budget with DNS by Pirozzoli & Bernardini (2011) at $(x-x_0)/\delta_0 = -0.14$. Normalization by free stream density, free stream velocity, and local boundary layer thickness. Solid lines, present LES; dashed lines, Pirozzoli DNS.

high-frequency fluctuations), which is a characteristic observed of the stochastic model presented by Touber & Sandham (2011).

Finally, in figure 11, contributions to the TKE budget are plotted at a streamwise station corresponding to the separation bubble in the interaction. While both the LES and DNS data are somewhat noisier than in the undisturbed boundary layer, we again see generally good agreement despite what appears to be a shifting trend towards the left in the LES turbulent transport and convective components. This may indicate that the average height of the separation bubble is somewhat less in the LES. Despite the differences that are observed, however, the present LES is found to be in generally good agreement with the DNS, which provides confidence in the use of our numerics for exploring the effects of parametric variation where no DNS data are available.

2.4.2. *Comparison with experiment*

Having established in the previous subsection that the baseline results are reasonably grid converged and agree well with existing DNS data, it is now desirable to further validate solution quality through comparison with available PIV data (Piponniau *et al.* 2009). However, as previous simulations (Hadjadj *et al.* 2010; Pirozzoli *et al.* 2010; Pirozzoli & Bernardini 2011) have found, the size of the separation bubble is often under-predicted with respect to the experiment. In the present simulations, this result is no different. It is convenient for experimentalists to measure the interaction length scale L_{int} as the difference between the inviscid impingement point x_0 and the approximate start of the reflected shock if it were extended to the wall. (Note that this length scale should not be confused with the separation length scale L_{sep}, which measures the difference between the points of separation and reattachment, as determined by the skin friction.) In the present refined simulation STD-L4-2300-8.0 as well as in the higher-Reynolds-number simulation STD-L2-4800-8.0, the interaction length is approximately $L_{int}/\delta_0 = 2.90$. As shown previously by figure 8, this value agrees quite well with DNS results; however, the experimental interaction length scale is actually $L_{int}/\delta_0 = 4.18$. When coordinates are scaled by the interaction length scale, however, good qualitative agreement with experiment is observed, as illustrated by figure 12.
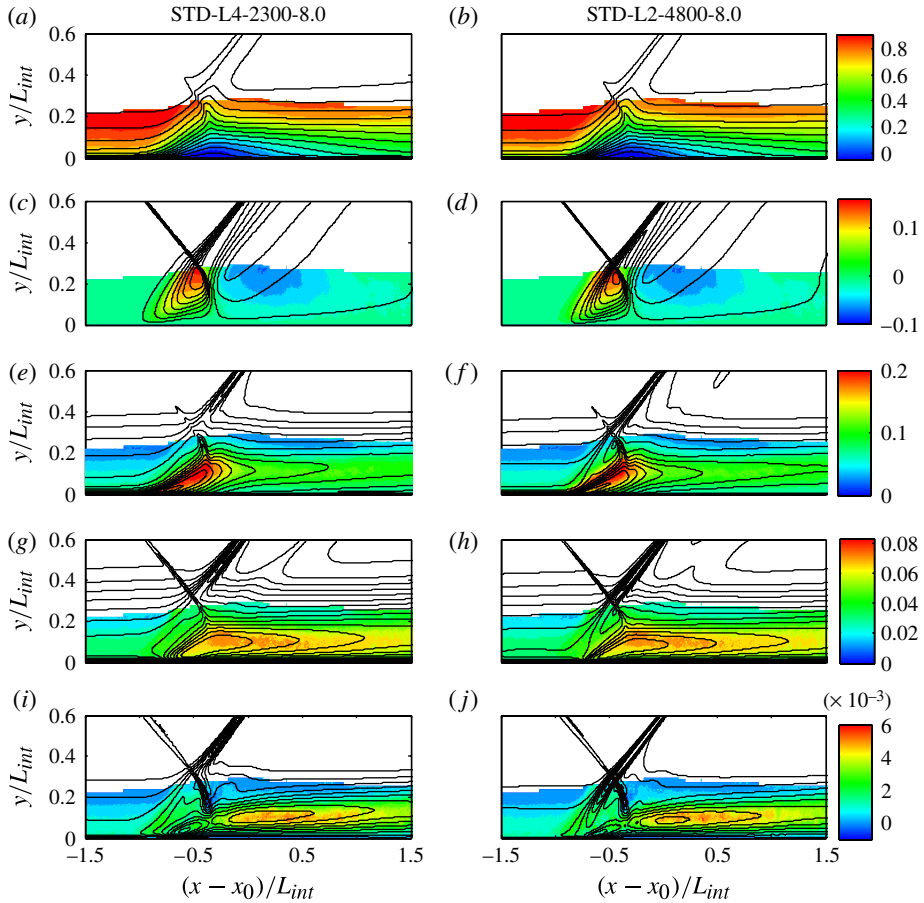
FIGURE 12. Mean and r.m.s. velocity distributions from simulation (lines) and PIV data by Piponniau *et al.* (2009) (colour contours). Plots (*a,c,e,g,i*) compare results at L4 resolution and $Re_\theta = 2300$; plots (*b,d,f,h,j*) compare results at L2 resolution and $Re_\theta = 4800$. Fifteen equally spaced contours of (*a,b*) $\bar{u}/u_\infty$ from -0.05 to 0.908, (*c,d*) $\bar{v}/u_\infty$ from -0.1 to 0.16, (*e,f*) $(\overline{u'u'})^{1/2}/u_\infty$ from 0 to 0.2, (*g,h*) $(\overline{v'v'})^{1/2}/u_\infty$ from 0 to 0.09, and (*i,j*) $-\overline{u'v'}/u_\infty^2$ from -0.001 to 0.006.

More quantitative comparisons with experiment are illustrated in figures 13 and 14. These figures plot, respectively, profiles of mean velocity and Reynolds stress components at 11 streamwise stations through the interaction. Mean flow profiles in figure 13, as expected, demonstrate good agreement with experiment and illustrate a high level of grid convergence between the L2 and L4 grid resolutions. The Reynolds stress components plotted in figure 14 are more sensitive and indicate some fairly minor discrepancies between simulation and experiment. In particular, profiles in the recovering boundary layer downstream of the interaction show the greatest level of disagreement with the experiment and simulations at $Re_\theta = 2300$; it is likely, however, that these differences are a result of differences in Reynolds number affecting the growth rate of the recovering boundary layer, as results from the STD-L2-4800-8.0 simulation indicate better agreement with experiment at these locations. Similarly, the reduced Reynolds number simulations appear to slightly over-estimate the Reynolds
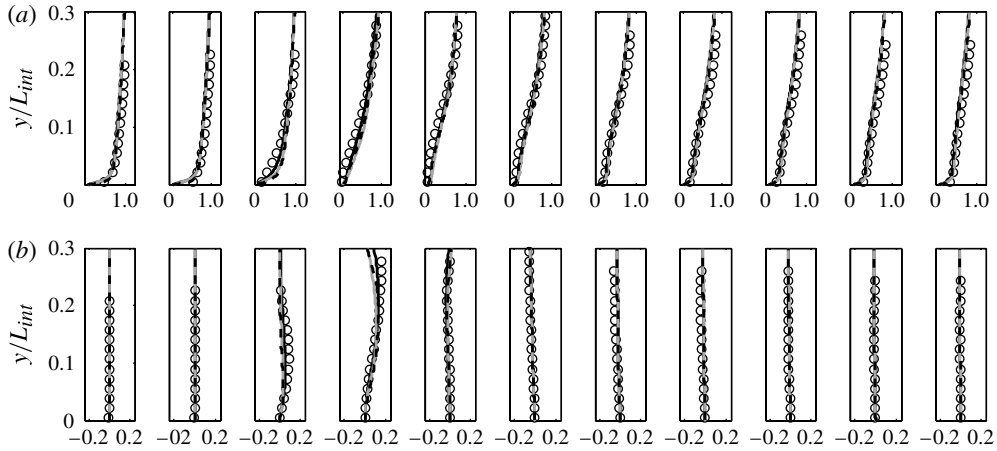
FIGURE 13. Comparison of mean velocity profiles with experiment: (*a*) $\overline{u}/u_\infty$; (*b*) $\overline{v}/u_\infty$. From left to right: $(x - x_0)/L_{int} = -1.5, -1.0, -0.75, -0.5, -0.25, 0.0, 0.25, 0.5, 0.75, 1.0, 1.5$. Symbols, PIV data by Piponniau *et al.* (2009); solid black, STD-L4-2300-8.0; solid grey, STD-L2-2300-8.0; dashed black, STD-L2-4800-8.0.

FIGURE 14. Comparison of Reynolds stress profiles with experiment: (*a*) $\left(\overline{u'u'}\right)^{1/2}/u_\infty$; (*b*) $\left(\overline{v'v'}\right)^{1/2}/u_\infty$. (*c*) $-\overline{u'v'}/u_\infty^2$. From left to right: $(x - x_0)/L_{int} = -1.5, -1.0, -0.75, -0.5, -0.25, 0.0, 0.25, 0.5, 0.75, 1.0, 1.5$. Symbols, PIV data by Piponniau *et al.* (2009); solid black, STD-L4-2300-8.0; solid grey, STD-L2-2300-8.0; dashed black, STD-L2-4800-8.0.
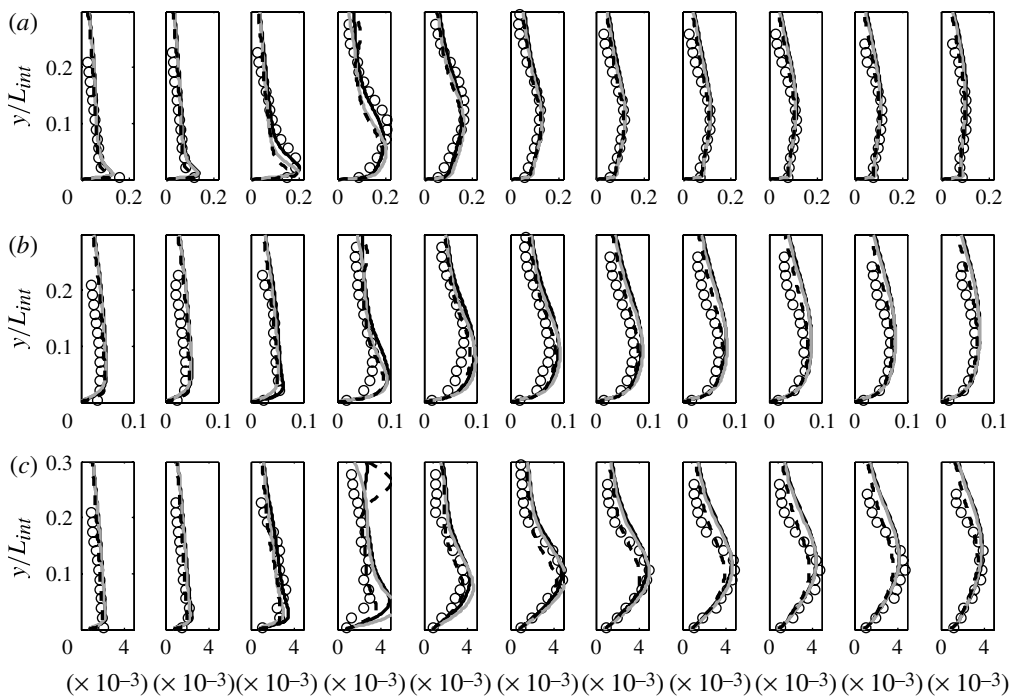
shear stress near the wall at the $(x - x_0)/L_{int} = -0.5$ station, which corresponds roughly with the point of initial separation, x_{sep}, in the simulation. Otherwise, quite good quantitative agreement is observed with experiment.

3. Results

Having outlined the numerics and established confidence in the quality of the baseline solution in §2, we now proceed with our investigation of OSTBLI physics using the LES database. First, in §3.1, trends in mean flow characteristics and conservation budgets are extracted with respect to variations in flow conditions (Reynolds number and shock strength) which may, in general, be uncertain. Next, in §3.2, several potential mechanisms that have been proposed as the cause of low-frequency unsteadiness are analysed. Finally, in §3.3, LES results are compared to RANS simulations of the same phenomenon. Utilizing the validated baseline solution as a *surrogate-truth model*, conclusions are drawn regarding the appropriateness of RANS modelling assumptions.

3.1. *Parametric variation*

Previous simulations (Hadjadj *et al.* 2010; Pirozzoli *et al.* 2010), including the present baseline and comparison DNS (Pirozzoli & Bernardini 2011), have found that when utilizing spanwise periodic boundary conditions, the interaction length scale L_{int} (that is, the difference between the inviscid impingement point x_0 and the approximate start of the reflected shock extended to the wall) and by extension the length of separation L_{sep} are often under-predicted with respect to experiment. In some instances, this discrepancy has been attributed to a difference in Reynolds number. Indeed, the present baseline simulation and comparison DNS have both been performed at $Re_\theta = 2300$, while the comparison experiment (Piponniau *et al.* 2009) has been performed at $Re_\theta = 5100$. Pirozzoli & Bernardini (2011) argue that since there exists a proportionality between non-dimensional shock strength $\mathscr{P} = \Delta p/2\tau_{w0}$ and interaction length (Dupont *et al.* 2006), interactions at higher Reynolds numbers (which necessarily have lower incoming wall shear stress) should result in longer interaction length scales. Note that a factor of 2 is used in the denominator of the definition of $\mathscr{P}$ for compatibility with Dupont *et al.* (2006). We thus begin our study of parametric variation by briefly considering the role that Reynolds number plays on mean flow characteristics, before investigating in more detail the effect of increasing shock strength via wedge angle.

Figure 15 shows skin friction and wall pressure across the interaction from simulations with consistent Δ^+ grid spacing and wedge angle but with varying Reynolds numbers. Recall that the L2 mesh resolution used here is based on viscous wall units at a given Reynolds number; thus, as Re_θ is increased, the number of grid points is additionally increased to maintain the same level of viscous wall unit resolution, as described in table 4 in the Appendix Based on this, we expect to have the same degree of convergence at $Re_\theta = 1500$ and 4800 (where no DNS data are available) as was previously demonstrated for $Re_\theta = 2300$. Recalling figure 8, it is therefore important to consider that while fine details in skin friction indicated some grid sensitivity at L2 resolution, length of separation was found to be mostly insensitive. As expected, it is observed that increasing the Reynolds number decreases the skin friction of the incoming boundary layer. Secondly, as the Reynolds number is increased, the qualitative behaviour of the skin friction curve between separation and reattachment appears to change; this behaviour is also reflected in the inflection

Simulation	$\dfrac{(x_{sep} - x_0)}{\delta_0}$	$\dfrac{(x_{ret} - x_0)}{\delta_0}$	L_{sep}/δ_0	L_{int}/δ_0	$\dfrac{L_{sep}}{L_{int}}$	h/δ_0	h^+
STD-L2-1500-8.0	−2.01	−0.67	1.34	2.79	0.48	2.19×10^{-2}	8.01
STD-L2-2300-8.0	−2.05	−0.77	1.28	2.91	0.44	1.05×10^{-2}	4.71
STD-L2-4800-8.0	−2.19	−0.58	1.61	3.02	0.53	0.86×10^{-2}	7.30
Pirozzoli DNS ($Re_\theta = 2300$)	−2.33	−0.72	1.61	2.89	0.56	—	—

TABLE 1. Variation in size of interaction as a function of Reynolds number: x_{sep} and x_{ret} denote, respectively, the points of mean separation and reattachment as determined by skin friction; L_{sep} indicates the length of separation ($x_{ret} - x_{sep}$), and L_{int} indicates the interaction length scale (the difference between the inviscid impingement point x_0 and the approximate start of the reflected shock extended to the wall). The maximal bubble height, h, is computed from the mean dividing streamline.
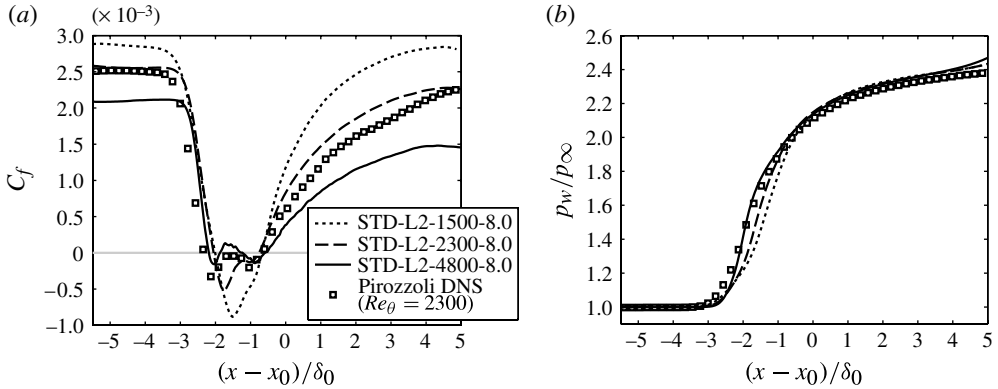
FIGURE 15. Effect of Reynolds number on separation bubble: (*a*) skin friction coefficient, and (*b*) wall pressure.

of the wall pressure curve. In particular, as Reynolds number is increased, the magnitude of the first negative skin friction peak decreases, and the second negative skin friction peak becomes more resolved. In fact, in the case of the STD-L2-4800-8.0 simulation (which is quite close to the experimental Reynolds number), there appear to be two completely separate separation bubbles. However, we also notice that the size of the separation bubble does not appear to be significantly affected by Reynolds number, which is consistent with observations made by Souverein (2010), who compared a high-Reynolds-number OSTBLI experiment conducted at TUD ($Re_\theta = 50\,000$, $M_\infty = 1.69$, $\phi = 6.0°$, $p_2/p_\infty = 1.35$) with a low-Reynolds-number experiment conducted at IUSTI ($Re_\theta = 5000$, $M_\infty = 2.28$, $\phi = 5.5°$, $p_2/p_\infty = 1.39$) and found L_{int}/δ_0 to be between 2.2 and 2.3 in each case. In regard to the scaling argument given by Pirozzoli & Bernardini (2011), it should be noted that the proportionality described by Dupont *et al.* (2006) was based on an experimental study in which the interaction parameter $\mathscr{P}$ was varied by changing the wedge angle – not by varying Reynolds number. It is therefore concluded that, at least over the range of Reynolds numbers considered in the present study, incoming skin friction is less important than shock strength in determining separation bubble size.

Attention is now turned to the role of shock strength in the physics of OSTBLI. For this investigation, conclusions are drawn primarily from seven simulations conducted at $Re_\theta = 1500$. These simulations, which are summarized in table 2, were conducted such that each simulation was provided the same realizations of inflow turbulence, and statistics are collected over a total time integration of 1419 δ_0/u_∞. In figure 16, skin friction and wall pressure profiles are plotted across the interaction at simulations with consistent Δ^+ spacing and Reynolds number for seven different wedge angles, ranging from weak separation with a 6.5° shock generator to strong separation with a 9.5° wedge. In order to ensure that the pressure profiles in figure 16 are unaffected by outflow boundary conditions, an additional double-length (LONG) simulation was run with a 9.5° wedge angle which indicated no significant effect due to domain size (Morgan 2012). As expected, it is observed that the stronger incident shocks result in greater separation. By observing the distance between curves, it is also clear that the relationship between wedge angle and separation length does not appear to be linear; that is, the intensity of the interaction appears to increase quite rapidly as the wedge angle is increased beyond a certain level. Perhaps unexpectedly, neither the minimum
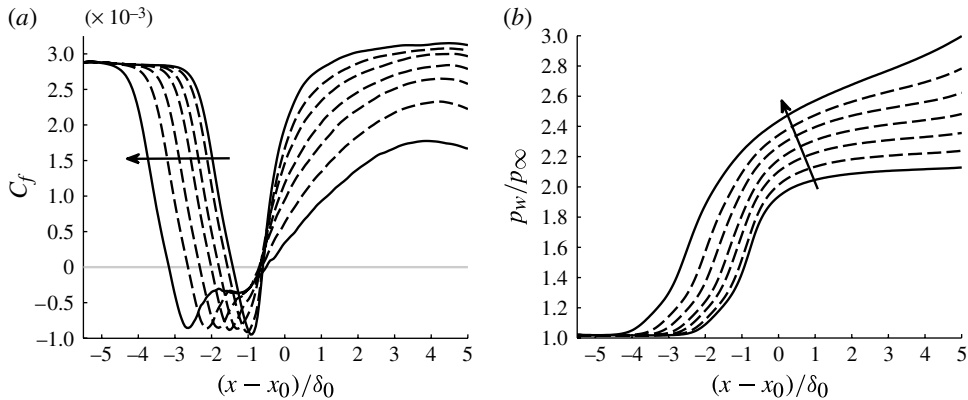
FIGURE 16. Effects of shock strength on separation bubble for simulations STD-L2-1500-6.5 through STD-L2-1500-9.5: (*a*) skin friction coefficient, and (*b*) wall pressure. Arrows indicate direction of increasing wedge angle from 6.5 to 9.5°.

Simulation	$\dfrac{(x_{sep} - x_0)}{\delta_0}$	$\dfrac{(x_{ret} - x_0)}{\delta_0}$	L_{sep}/δ_0	L_{int}/δ_0	$\dfrac{L_{sep}}{L_{int}}$	h/δ_0	h^+
STD-L2-1500-6.5	-1.42	-0.59	0.83	2.49	0.33	2.22×10^{-2}	8.12
STD-L2-1500-7.0	-1.57	-0.60	0.97	2.55	0.38	2.21×10^{-2}	8.08
STD-L2-1500-7.5	-1.80	-0.66	1.14	2.61	0.44	2.15×10^{-2}	7.86
STD-L2-1500-8.0	-2.01	-0.67	1.34	2.79	0.48	2.19×10^{-2}	8.01
STD-L2-1500-8.5	-2.32	-0.69	1.64	3.14	0.52	2.14×10^{-2}	7.83
STD-L2-1500-9.0	-2.65	-0.63	2.02	3.46	0.58	2.19×10^{-2}	8.01
STD-L2-1500-9.5	-3.17	-0.50	2.67	3.83	0.70	2.84×10^{-2}	10.4

TABLE 2. Variation in size of interaction as a function of wedge angle: x_{sep} and x_{ret} denote, respectively, the points of mean separation and reattachment as determined by skin friction; L_{sep} indicates the length of separation ($x_{ret} - x_{sep}$), and L_{int} indicates the interaction length scale (the difference between the inviscid impingement point x_0 and the approximate start of the reflected shock extended to the wall). The maximal bubble height, h, is computed from the mean dividing streamline.

skin friction nor the location of the reattachment point appear to be significantly affected by shock strength, although the latter observation is probably a result of maintaining the inviscid shock impingement location, x_0, consistent for all simulations. It is also interesting to note that for wedge angles above ~8.0°, the 'plateau' feature in the skin friction curve appears to become more pronounced. The significance of this feature is not immediately clear; however, it probably has to do with the incipient nature of separation associated with weaker incident shocks.

With the database of the LES results presented, it is now possible to better consider the scaling of the interaction length scale. As previously mentioned, the first OSTBLI experimental studies at IUSTI by Dupont *et al.* (2006) treated interaction length as a function of $\mathscr{P}$ (pressure rise over shear stress). However, later work by Souverein (2010) has indicated that this simple scaling may not adequately collapse data taken at significantly different Reynolds numbers, a result which is consistent with the present

investigation. Souverein (2010) suggested instead that the length scale should be scaled by displacement thickness and a function of the shock strength, $g_3(\phi, \beta)$, and that this interaction length scale should vary as a function of the potential flow; as originally formulated by Souverein (2010), the function g_3 is defined by

$$g_3(\phi, \beta) = \frac{\sin(\beta - \phi)}{\sin(\beta)\sin(\phi)}, \tag{3.1}$$

where ϕ indicates the wedge angle and β indicates the shock angle.

Jaunet, Debieve & Dupont (2012), however, have recently concluded that the potential flow function utilized by Souverein (2010) is insufficient to adequately capture the effect of wall heating, and work by Morgan (2012) has shown that scaling proposed by Jaunet *et al.* (2012) is again insufficient to capture Reynolds number effects. Thus, to assess interaction length scale scaling in the present work, basic dimensional analysis is first invoked. Drawing on the results of these previous studies and the collected body of knowledge surrounding OSTBLI phenomena, we begin our dimensional analysis by assuming that the interaction length scale should be a function of the potential flow conditions, the shock strength, the wall temperature, the adiabatic wall temperature (T_{aw}), the wall shear stress, and the boundary layer displacement thickness; this statement is expressed functionally by

$$L_{int} = \Phi\left(u_\infty, \rho_\infty, \mu_\infty, \Delta p, T_w, T_{aw}, \tau_w, \delta^*\right). \tag{3.2}$$

Notice that the interaction is assumed to be a function of displacement thickness, δ^*, rather than the momentum thickness. This result derives from analysis by Souverein (2010), who found little difference when applying scaling arguments based on either mass conservation or on momentum conservation. If the classical 'Π theorem' by Buckingham (1914) is invoked, it is easily shown that the non-dimensional length scale may be expressed instead as a function of four non-dimensional parameters, including a coefficient of pressure ($C_p = \Delta p/(\rho_\infty u_\infty^2/2)$), the ratio of the wall temperature to the adiabatic wall temperature, the Reynolds number based on displacement thickness, and the skin friction coefficient, as expressed by

$$\frac{L_{int}}{\delta^*} = \Phi\left(C_p, \frac{T_w}{T_{aw}}, Re_{\delta^*}, C_f\right). \tag{3.3}$$

This is, of course, only one choice of several valid sets of non-dimensional parameters describing the OSTBLI system. However, the present collection of parameters is selected because it may be used to describe a relationship between the non-dimensional length scale and a non-dimensional shock strength. To establish such a relationship, one might be tempted to consider the limit as $Re_{\delta^*} \to \infty$ and to draw on the results of triple deck theory (Stewartson 1974). However, as the present analysis concerns interactions at relatively low Reynolds number, it is believed that such scaling would be inappropriate. Therefore, we begin by assuming the form of a power law monomial in order to determine an empirical relationship. Thus, the problem of proper scaling is reduced to finding the exponents α_1, α_2 and α_3 that best collapse the length scale $\hat{L}$ against the interaction strength parameter $\hat{\mathscr{P}}$, where $\hat{L}$ and $\hat{\mathscr{P}}$ are given explicitly by

$$\hat{L} = \frac{L_{int}}{\delta^* g_3(\beta, \phi)}, \quad \hat{\mathscr{P}} = C_p\left(\frac{T_w}{T_{aw}}\right)^{\alpha_1}(Re_{\delta^*})^{\alpha_2}\left(C_f\right)^{\alpha_3}. \tag{3.4}$$
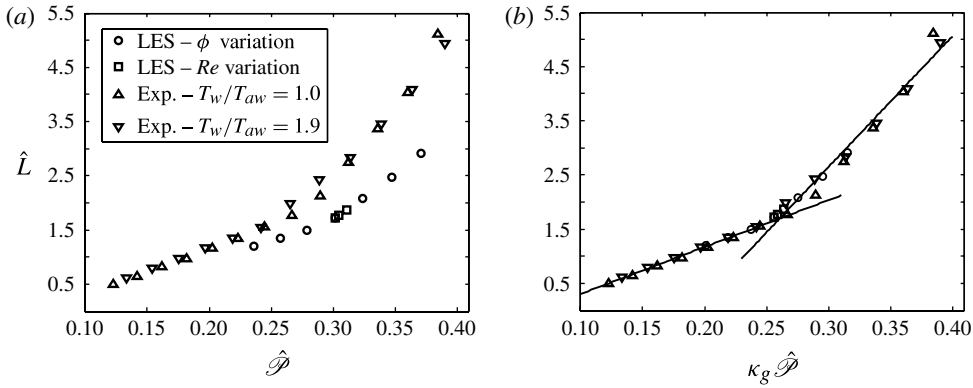
FIGURE 17. Scaling of interaction length scale. $\hat{\mathscr{P}} = C_p(T_w/T_{aw})^{-1/10}(C_f)^{1/10}$. (*a*) Raw comparison with experimental data by Jaunet *et al.* (2012). (*b*) Scaling with geometrical correction factor.

Note that the power on C_p is chosen to be unity in order to emphasize interpretation of the horizontal scaling as a non-dimensional shock strength.

Utilizing the experimental results by Jaunet *et al.* (2012) to determine α_1 and the present LES results to determine α_2 and α_3 (as discussed in greater detail by Morgan 2012) yields two valid scalings. In the first scaling, $\alpha_1 = -1/10$, $\alpha_2 = -1/40$ and $\alpha_3 \to 0$; in the second scaling, $\alpha_1 = -1/10$, $\alpha_3 = 1/10$ and $\alpha_2 \to 0$. This fact suggests that the effects of Reynolds number and skin friction may be combined into a single parameter. It is further encouraging to note that when comparing the two valid scalings $\alpha_2 = -(\alpha_3/4)$, which is a result consistent with the empirical relationship suggested by Blasius (1913), in which skin friction in the undisturbed boundary layer is expected to scale like $Re_\theta^{-1/4}$. To simplify the present analysis, then, the second scaling is selected such that the dependence on Reynolds number is dropped, and assumed to be absorbed by the dependence on skin friction. Although this proposed scaling, illustrated in figure 17(*a*), appropriately collapses each data set individually, there still remains a disparity between the experimental data and the LES data. As discussed previously, however, the spanwise periodic simulations are known to under-predict the size of separation with respect to experiment. If this discrepancy is accounted for by introducing an empirical factor $\kappa_g = 0.85$ to the scaling of the simulation results, as shown by figure 17(*b*), the two data sets show excellent collapse.

The effect of parametric variation on the analysis of conservation budgets in the interaction is considered next. It is expected that such data may be useful when analysing or improving lower-fidelity models (the subject of § 3.3) or in the analysis of low-frequency dynamics (the subject of § 3.2). In particular, attention is focused on the balance of terms in the Navier–Stokes momentum equations

$$\frac{\partial}{\partial t}(\overline{\rho}\widetilde{u}_i) = -\frac{\partial}{\partial x_j}(\overline{\rho}\widetilde{u}_i\widetilde{u}_j) - \frac{\partial \overline{p}}{\partial x_i} + \frac{\partial}{\partial x_j}\left(\overline{\sigma}_{ij} - \overline{\rho}\widetilde{u_i''u_j''}\right) \tag{3.5}$$

(as presented by Huang, Coleman & Bradshaw 1995), as well as the TKE equation described earlier (equation (2.1)). Note that the mass continuity equation is not considered here because this equation contains no turbulence terms in the context of
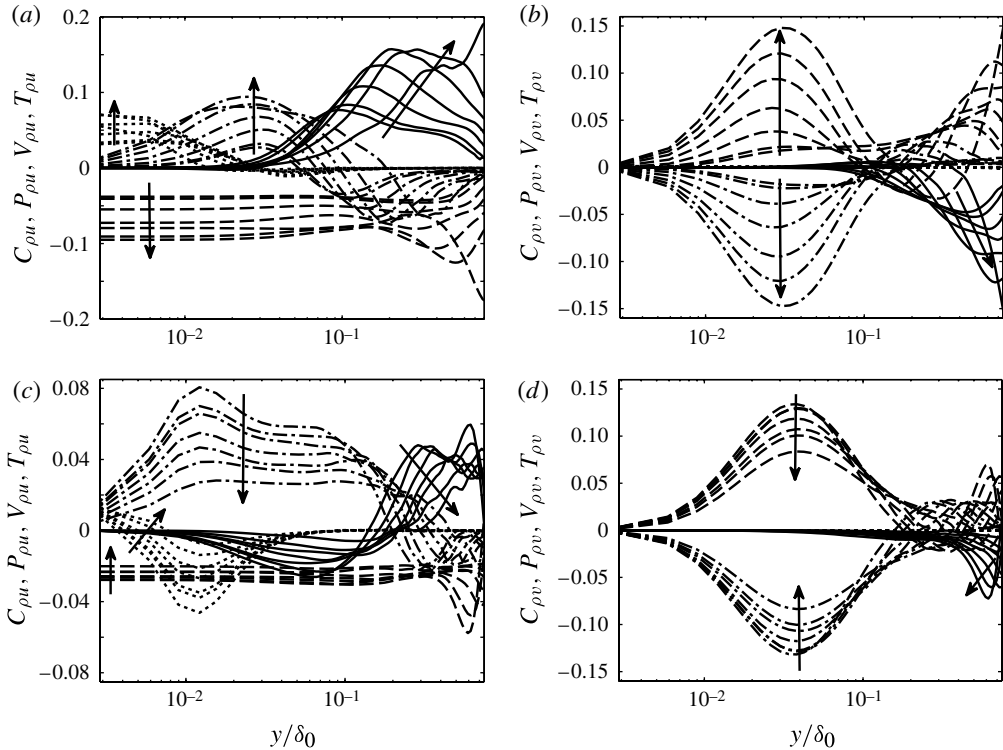
FIGURE 18. Change in momentum budget terms as a function of wedge angle: (a,c) streamwise momentum, (b,d) wall-normal momentum; (a,b) $(x - x_0)/L_{int} = -0.60$, (c,d) $(x - x_0)/L_{int} = 0.00$. Arrows indicate direction of increasing wedge angle from 6.5 to 9.5°. Solid, C; dashes, P; dots, V; dashes and dots, T. Maximum residual imbalance: $+/-0.001$.

Favre-averaged mean flow. Nor is the internal energy budget considered here because heat transfer in this particular problem is minimal in comparison to momentum effects; however, this analysis may be found in Morgan & Lele (2011).

Denoting the right-hand side terms in (3.5) (moving from left to right) by C, P, V and T, which indicate, respectively, the contributions due to convection, pressure, viscous diffusion, and turbulent transport, we now plot in figure 18 the streamwise and wall-normal momentum budgets at $(x-x_0)/L_{int} = -0.60$ and 0.00. First, by considering the streamwise momentum budgets, it is observed that all four terms are active in the inner boundary layer region, with the greatest contribution due to turbulent transport and the viscous contribution approaching zero around $y/\delta_0 \approx 0.08$. It is also interesting to note that upstream of the impinging shock foot, there is a trend of increasing magnitude with increasing shock strength, while downstream this trend reverses. This may seem somewhat counter-intuitive at first; however, it is likely a result of the shock foot being closer to the wall in the case of the smaller wedge angle. That is, greater wedge angles create greater separation, which results in the sonic line rising away from the wall with increased wedge angle. Thus, at $(x - x_0)/L_{int} = 0.00$, terms related to total stress (viscous stress + Reynolds stress) balance the pressure gradient near the wall, and this total should be greater for smaller wedge angles due to faster downstream recovery rates, as shown by figure 16. In the wall-normal accounting,
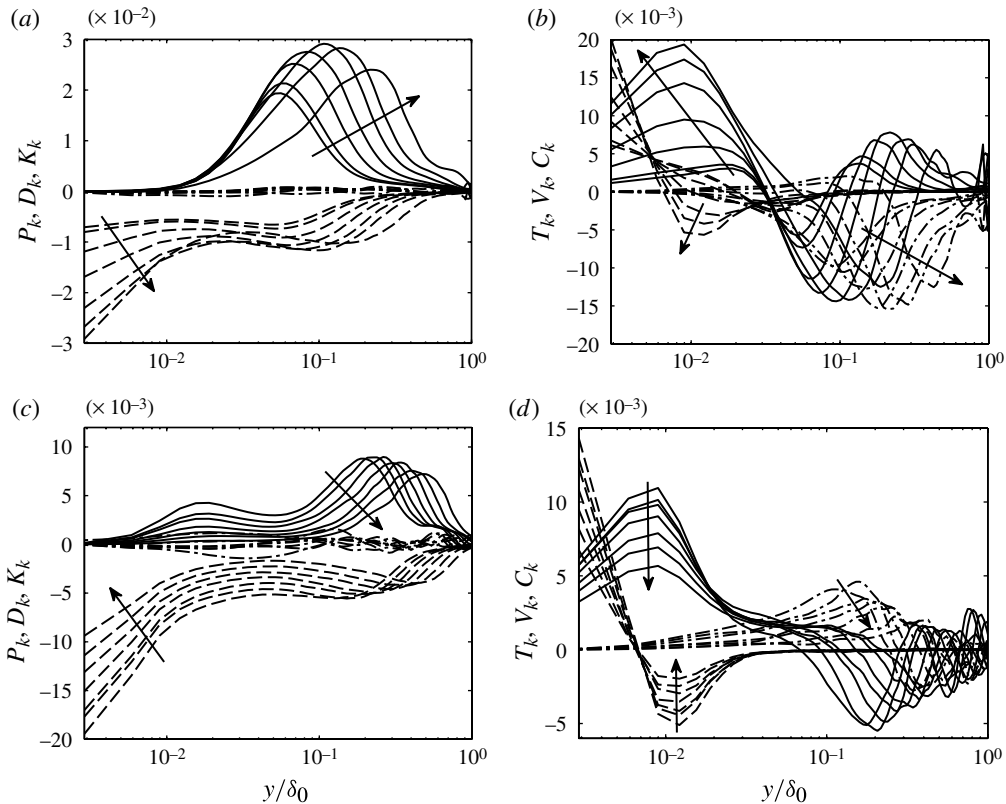
FIGURE 19. Change in turbulence kinetic energy budget terms as a function of wedge angle: (*a,b*) $(x - x_0)/L_{int} = -0.60$, (*c,d*) $(x - x_0)/L_{int} = 0.00$. Arrows indicate direction of increasing wedge angle from 6.5 to 9.5°. (*a,c*) Solid, P_k; dashes, D_k; dashes and dots, K_k. (*b,d*) Solid, T_k; dashes, V_k; dashes and dots, C_k. Maximum residual imbalance: $+/-0.0025$.

however, the viscous term is negligible, and the convective and turbulent transport terms balance each other for most of the boundary layer thickness, with the convective term playing a role only near the shock.

Turning now to the turbulence kinetic energy budget described by (2.1), figure 19 plots the variation in TKE terms with increasing wedge angle. As done previously, the terms are divided into two plots for clarity, with contributions from production (P_k), dissipation (D_k), and compressibility (K_k) illustrated separately from contributions due to turbulent transport (T_k), viscous diffusion (V_k), and convection (C_k). Again, the familiar trend is observed of increasing magnitude with wedge angle at the upstream location and decreasing magnitude downstream. It is also notable that in the inner boundary layer, all terms except convection appear to contribute significantly to the budget. The convective term appears to be important only in the outer boundary layer (and in fact changes signs between the upstream and downstream locations), whereas the viscous diffusion term appears to be important only in the inner boundary layer. Additionally, while there is some noise in the contribution due to compressibility terms, it appears that K_k is generally small enough to be disregarded as negligible. By comparing our STD-L2-1500-8.0 results with the baseline STD-L2-2300-8.0 results
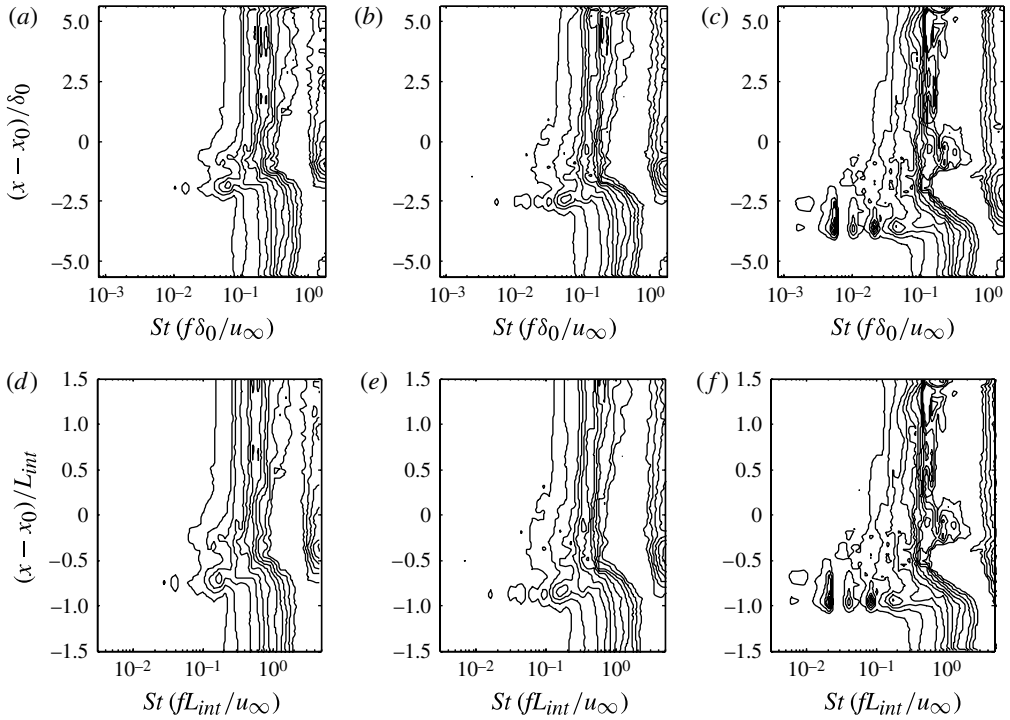
FIGURE 20. Compensated wall pressure spectra ($fE(f)$) for simulations STD-L2-1500-(6.5, 8.0, 9.5). Spectra are normalized such that at each streamwise station, the integral over frequency is unity. 12 contour levels are shown, from 0 to 0.6. Plots (a–c) are normalized by δ_0, and (d–f) are normalized by L_{int}; (a,d) $\phi = 6.5°$, (b,e) $\phi = 8.0°$, (c,f) $\phi = 9.5°$.

(shown in figure 7), the apparent effect of increasing Reynolds number is to generally increase the peak magnitudes while simultaneously shifting the location of peak values closer to the wall.

The effect of wedge angle variation on low-frequency unsteadiness is considered in figure 20. In figure 20(a–c), compensated wall pressure spectra (that is, the energy spectral density of wall pressure fluctuations, pre-multiplied by the frequency and normalized to integrate to unity) are plotted for three wedge angles, with normalization by the undisturbed boundary layer thickness, δ_0, and free stream velocity, u_∞; in figure 20(d–f), these plots are repeated with length scales normalized by L_{int}. When normalized by the constant δ_0, as in figure 20(a–c), it is observed that the location of the characteristic low-frequency peak occurs approximately at the location of initial separation in each case and that, consistent with figure 16, this location moves upstream with an increase in shock strength. Furthermore, when scaling by δ_0, it appears that the time scale of the low-frequency peak shifts out towards lower frequencies, which is consistent with simulations performed by Pirozzoli *et al.* (2010). On the other hand, by choosing L_{int} to scale the spatial dimension, as in figure 20(d–f), one may account for the larger scale of interaction with increased shock strength. Although this scaling essentially fixes the location of the low-frequency peak in the streamwise dimension, it makes clear the fact that the strongest interaction contains energy at lower frequencies, even when the increased

interaction length scale is taken into account. This trend may also be true between the 6.5 and 8.0° interactions, although the evidence is somewhat less conclusive. As Piponniau *et al.* (2009) and Souverein (2010) have conjectured, there may be a change in the dominant mechanism behind low-frequency oscillations when moving from the incipient to the strongly separated regime. Although the mean flow is separated in each of the simulations presently considered, as we report in Morgan, Kawai & Lele (2011*a*), the maximum probability of flow reversal in the 8.0° case, even along the wall beneath the impinging shock foot, remains near 60 %. Thus, the shift toward lower frequencies that is observed with increased shock intensity may be due to the change in the interaction dynamics that is observed when moving away from the incipient regime and towards the strongly separated regime. Recalling that all three simulations were provided identical realizations of inflow turbulence, it additionally seems unlikely that the low-frequency motions should be purely a response to forcing (either through the interaction with long coherent structures or unintentionally through the recycling/rescaling procedure) in the undisturbed boundary layer. The mechanism behind low-frequency unsteadiness will be explored in greater detail in § 3.2.

3.2. *Investigation of low-frequency motion*

Attention is now turned to the governing mechanism behind low-frequency unsteadiness in OSTBLI. Our approach is to utilize the present LES database to assess some of the most commonly cited mechanisms that have been proposed. In particular, it is the intention of this section to investigate causal mechanisms suggested by Pirozzoli & Grasso (2006), Ganapathisubramani *et al.* (2009) and Piponniau *et al.* (2009). To begin, the model described by Piponniau *et al.* (2009) is considered, which proposes the following mechanism. First, eddies are formed in the mixing layer near the separation point and grow as they move downstream. These eddies entrain some fluid from the separated zone into the mixing layer, and after some distance, the eddies are shed downstream, bringing with them the mass, momentum, and vorticity that has been entrained. This action generates a deficit of mass in the separation bubble that increases over time, which must be re-introduced into the bubble. Using a simplified geometric description of the separation bubble, Piponniau *et al.* (2009) then calculate that the time scale over which this re-introduction of mass takes place should be on the same order as the low-frequency oscillations. To assess this model, our approach is to compute the time history of the mass and momentum conservation equations integrated over the spanwise averaged separation bubble and surrounding area. In this way, we expect to quantitatively describe the transfer of mass and momentum between the separation bubble and surrounding area and to analyse the time scale of dynamics in the separation bubble to determine if it is in agreement with the model described by Piponniau *et al.* (2009). For this investigation, a time record from the STD-L2-2300-8.0 database is utilized spanning 618 δ_0/u_∞ with instantaneous, spanwise averaged flow data sampled every 0.02736 δ_0/u_∞. In order to identify low-frequency behaviour in our data, a pseudo-Gaussian low-pass filter is applied to the time-varying signals of the budget terms.

The budgets of two control volumes are considered: one representing the separation bubble and another representing the more general *interaction zone*, which encompasses the area surrounding the separation bubble. The mass conservation equation for an arbitrary, moving control volume (CV) with a volume denoted by Ω and a boundary denoted by $\partial\Omega$ is given by (3.6) (see Morgan 2012 for the full derivation). In this equation, $\boldsymbol{v_c}$ indicates the local velocity of the control volume boundary, and $\hat{\boldsymbol{n}}$ denotes

the local outward normal:

$$\underbrace{\frac{\mathrm{d}}{\mathrm{d}t} \int_{\Omega} \bar{\rho} \, \mathrm{d}V}_{\text{mass flux term}} = \underbrace{-\oint_{\partial\Omega} \boldsymbol{r} \cdot \hat{\boldsymbol{n}} \, \mathrm{d}S}_{\text{convective term}} + \underbrace{\oint_{\partial\Omega} \bar{\rho} \left(\boldsymbol{v}_c \cdot \hat{\boldsymbol{n}} \right) \mathrm{d}S}_{\text{term due to unsteady CV}}. \quad (3.6)$$

For the spanwise averaged interaction, $\boldsymbol{r} = \{\bar{\rho}\tilde{u}, \bar{\rho}\tilde{v}\}$. For ease of notation, we will denote the mass flux term, the convective term, and the term due to unsteady CV motion by $\dot{M}_\rho$, C_ρ, and U_ρ^{CV}, respectively. Similarly, the streamwise momentum conservation equation is given by

$$\underbrace{\frac{\mathrm{d}}{\mathrm{d}t} \int_{\Omega} \bar{\rho}\tilde{u} \, \mathrm{d}V}_{\text{momentum flux}} = \underbrace{-\oint_{\partial\Omega} (\boldsymbol{b} + \boldsymbol{p} + \boldsymbol{v} + \boldsymbol{t}) \cdot \hat{\boldsymbol{n}} \, \mathrm{d}S}_{\text{convective term}} + \underbrace{\oint_{\partial\Omega} \bar{\rho}\tilde{u} \left(\boldsymbol{v}_c \cdot \hat{\boldsymbol{n}} \right) \mathrm{d}S}_{\text{term due to unsteady CV}}, \quad (3.7)$$

where $\boldsymbol{b} = \{\overline{\rho u \tilde{u}}, \overline{\rho u \tilde{v}}\}$, $\boldsymbol{p} = \{\bar{p}, 0\}$, $\boldsymbol{v} = \{-\overline{\sigma_{11}}, -\overline{\sigma_{12}}\}$, and $\boldsymbol{t} = \{\overline{\rho u'' u''}, \overline{\rho u'' v''}\}$. Integral relations of these terms represent, respectively, convective contributions due to bulk transport ($B_{\rho u}$), pressure ($P_{\rho u}$), viscous diffusion ($V_{\rho u}$), and turbulent transport ($T_{\rho u}$). To ease notation, we denote the momentum flux term and the term due to unsteady CV motion by $\dot{M}_{\rho u}$ and $U_{\rho u}^{CV}$; the convective term will be denoted by its aforementioned constitutive terms such that $C_{\rho u} = B_{\rho u} + P_{\rho u} + V_{\rho u} + T_{\rho u}$. Note that this notation is similar to the notation used in § 3.1 to describe pointwise momentum conservation components; in the present section, however, the previous notation is superseded with these definitions for integrated momentum conservation in a moving control volume.

The boundaries of the separation bubble are defined by the dividing streamline such that the momentum flux term is identically zero. Note, however, that instantaneously, there may be more than one set of closed curves defined by the dividing streamline; that is, there may be more than one bubble. Indeed, in the case of the 8.0° interaction, this is almost always true. To account for this fact, the terms in (3.6) are summed over all bubbles. To capture the dynamics of the area surrounding the separation bubble, we define the second control volume with a parabolic arc, as illustrated in figure 21, fitted through three control points. Its extent is defined by the two points on the wall where the skin friction coefficient, which has been smoothed with a 15-point pseudo-Gaussian smoothing filter, is equal to the average of the minimum and maximum values; that is, the extent is defined by the two points where $\hat{C}_f = (\hat{C}_{f,min} + \hat{C}_{f,max})/2$. The height of the arc is defined by a third point, chosen to approximate the depth of penetration of the impinging shock foot. This third point is selected by scanning in the y-direction for the highest point of the sonic line. As illustrated in figure 21, this choice of curve is defined such that the majority of the strong vorticity originating at the foot of the reflected shock is generated within the curve and exits through its leeward side. Additionally, the curve is defined such that peak TKE is captured within. By analysing the integrated budgets for both the separation bubble and the surrounding area (as defined by the parabolic arc segment just defined), we hope to probe for low-frequency transfer between the bubble itself and the surrounding shear layer.

Figure 22 plots the most significant contributions to the mass and momentum conservation budgets integrated over the separation bubble and interaction zone control volumes over a time history of 600 δ_0/u_∞. For reference, signals indicating the size of the separation (L_{sep}), the maximum TKE in the upstream boundary layer (k_{up}), and location of the reflected shock foot (x_{shk}) are also plotted. (The latter signal is determined by utilizing the pressure gradient magnitude as a shock sensor outside the boundary layer, performing a linear least-squares fit to the streamwise location of
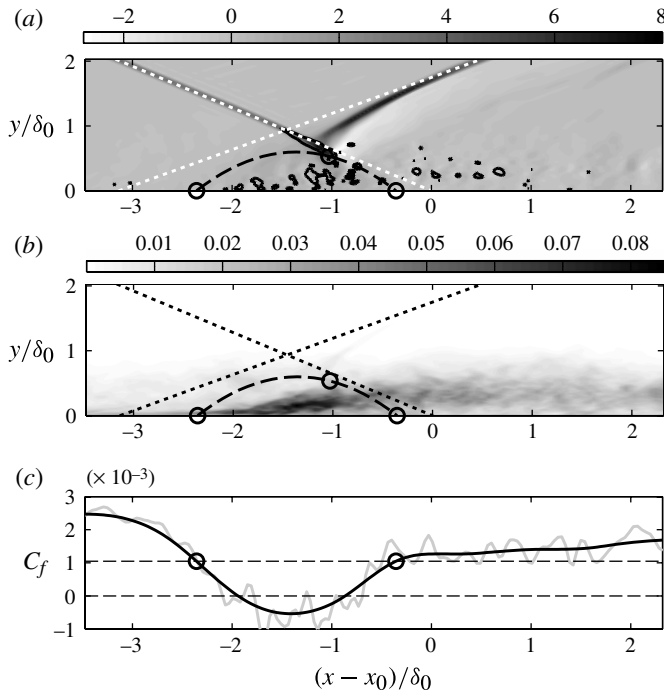
FIGURE 21. Definition of the interaction zone control volume. (*a*) The exterior control volume (dashed black) and control points (black circles) are superimposed on colour contours of $\mathrm{d}(p/p_\infty)/\mathrm{d}(x/\delta_0)$. Vortical structures defined by the Q-criterion are outlined in solid black, and shock positions are indicated by dotted white lines. (*b*) The exterior control volume (dashed black) and control points (black circles) are superimposed on colour contours of k/u_∞^2. Shock positions are indicated by dotted black lines. (*c*) The filtered skin friction coefficient, $\hat{C}_f$ (solid black) is superimposed on the raw coefficient (solid grey). Dashed black lines indicate $C_f = 0$ and $\hat{C}_f = (\hat{C}_{f,min} + \hat{C}_{f,max})/2$.

maximal pressure gradient, and extending this line to the wall.) Note that a low-pass filter with a cut-off frequency of 0.25 u_∞/δ_0 has been applied to all signals to aid in visualization, while maintaining the full low-frequency spectra. Considering first mass conservation in the separation bubble, it is observed that the mass flux $\dot{M}_\rho$ is balanced almost entirely by U_ρ^{CV}. In the momentum budget (where the flux term is zero due to the choice of the dividing streamline as the upper boundary), the convective contributions due to pressure ($P_{\rho u}$) and turbulent transport ($T_{\rho u}$) mostly balance, with some nearly constant contribution from viscous diffusion ($V_{\rho u}$). In the interaction zone, the same two terms balance in the mass equation; however, the momentum balance is different. While the separation bubble has a mean height of only 0.0324 δ_0/u_∞, the momentum bubble extends away from the wall up to the sonic line. Thus, it is seen in figure 22(*d*) that the pressure term is balanced by the bulk transport term ($B_{\rho u}$), rather than the turbulent transport term, as in the separation bubble. As expected, the momentum flux is non-zero in the interaction zone; however, this term is balanced exactly by the term due to CV motion ($U_{\rho u}^{CV}$). Although the additional reference signals are plotted here for general comparison only, some trends may already be identified; for instance, decreases in separation length are
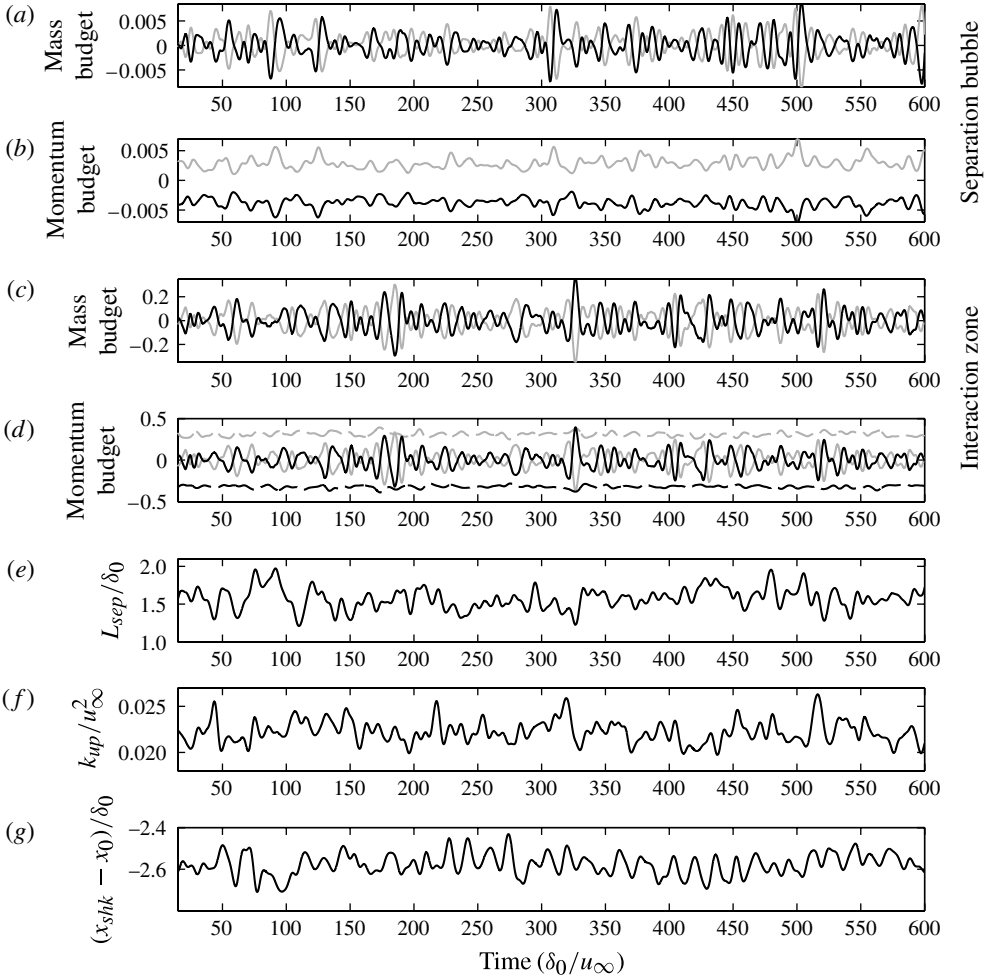
FIGURE 22. Integrated conservation budgets in moving control volumes. (a,c) Mass conservation budget: solid black, $\dot{M}_\rho$; solid grey, U_ρ^{CV}. (b) Streamwise momentum conservation budget: solid black, $P_{\rho u}$; solid grey, $T_{\rho u}$. (d) Streamwise momentum conservation budget: solid black, $\dot{M}_{\rho u}$; solid grey, $U_{\rho u}^{CV}$; dashed black, $P_{\rho u}$; dashed grey, $B_{\rho u}$. $(e$–$g)$ Time signals of separation length scale (L_{sep}), maximum TKE upstream of the interaction (at $(x-x_0)/\delta_0 = -3.5$), and reflected shock position, x_{shk}. All signals filtered using low-pass filter with cut-off frequency of $0.25\, u_\infty/\delta_0$.

generally preceded by increased upstream TKE. Similarly, decreases in upstream TKE generally precede upstream motion of the reflected shock foot. Correlations between shock motion and the upstream boundary layer are examined more rigorously later in this section when considering the superstructure theory of Ganapathisubramani *et al.* (2009). Attention is first turned to the mass entrainment model suggested by Piponniau *et al.* (2009).

In figure 23, an attempt is made to assess the role that mass deficit in the separation bubble may play in the low-frequency dynamics of the OSTBLI system. Temporal covariance between integrated density in the separation bubble ($M = \int_\Omega \bar{\rho}\, dV$) and
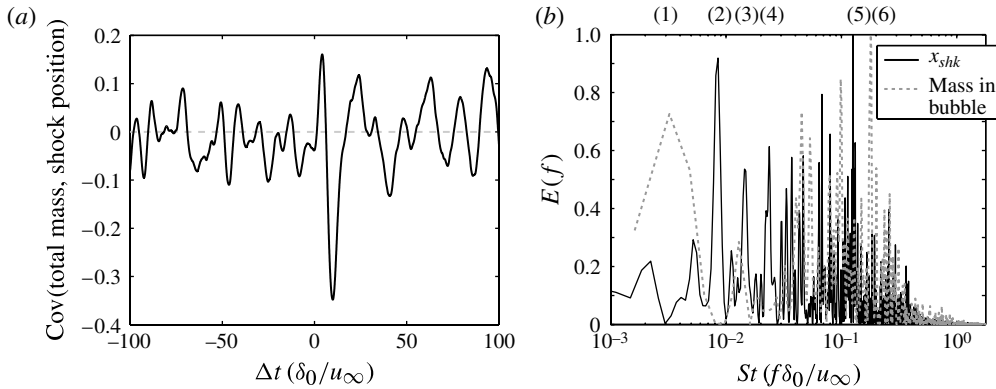
FIGURE 23. Spectral content of mass signal in the separation bubble. (*a*) Temporal covariance of shock position and total mass signals. (*b*) Energy spectral density ($E(f)$) of reflected shock position (x_{shk}) and $\int_{\Omega} \bar{\rho} \, dV$ integrated over separation bubble control volume. Signals are normalized by their maximal values. Indicated frequencies 1–6 correspond to $St \approx 0.00324, 0.00853, 0.0148, 0.0237, 0.126$ and 0.180.

the streamwise location of the reflected shock foot, x_{shk}, is plotted first. Here and elsewhere in the present work, the covariance function for two arbitrary signals s_1 and s_2 is defined by

$$\text{Cov}\,(s_1, s_2) = \frac{\overline{s_1' s_2'}}{\left(\overline{s_1' s_1'} \; \overline{s_2' s_2'}\right)^{1/2}}. \tag{3.8}$$

$$C_{s_1,s_2}(\Delta t) = \text{Cov}\,(s_1(t), s_2(t + \Delta t))\,. \tag{3.9}$$

The covariance function illustrated in figure 23 demonstrates that the two signals are negatively correlated with a time delay of $\Delta t = 9.93\delta_0/u_\infty$. This indicates that the x_{shk} signal tends to lag the total mass signal and that (due to the negative correlation), the shock tends to move upstream when the separation bubble contains more mass (and conversely move downstream when the bubble contains less mass). Since the wall-normal density gradient is not very large over the height of the bubble, it may be assumed that the change in mass is most likely a result of a change in bubble area, rather than due to compressibility effects.

To investigate the role that the observed correlation may play in low-frequency dynamics, figure 23 additionally plots the energy spectra of $\int_{\Omega} \bar{\rho} \, dV$ and of x_{shk}. From this comparison, it is observed that while the maximal peak for the x_{shk} signal occurs at a Strouhal number of 0.126 (with a low-frequency peak at $St = 0.00853$), the maximal peak for the mass signal occurs at a higher Strouhal number of 0.180. According to analysis by Piponniau *et al.* (2009), the frequency of the mass recovery in the separation bubble should be given by

$$St = \frac{f\delta_0}{u_\infty} = \Phi(M_c)g(r, s)\frac{\delta_0}{h}, \tag{3.10}$$

where $\Phi(M_c)$ indicates the normalized spreading rate of a subsonic half jet (a function of isentropic convective Mach number), $g(r, s)$ is a function of the velocity and density ratios (r and s, respectively) across the shear layer, and h is the height of

the separation bubble as defined by the dividing streamline. Following the procedure utilized by Piponniau *et al.* (2009) to determine Φ, we observe that for free stream Mach numbers greater than 2, $M_c \approx 1.0$. Drawing from the normalized spreading rate described by Smits & Dussauge (2006), we have $\Phi(M_c = 1) \approx 0.3$. Next, drawing from our LES database, we determine $r \approx -0.012$ and $s \approx 0.531$, from which can be computed $g(r, s) \approx 0.0192$. Finally, the mean height of the separation bubble in LES is computed as $h/\delta_0 = 0.0324$. Taking $\Phi(M_c) = 0.3$, $g(r, s) = 0.0192$, and $h/\delta_0 = 0.0324$, (3.10) predicts that the Strouhal number associated with mass recovery in the separation bubble should be 0.178, which is in excellent agreement with the observed maximal frequency in figure 23. The fact that (3.10) is able to accurately predict the frequency associated with the mass in the separation bubble is strongly indicative that the mass entrainment mechanism described by Piponniau *et al.* (2009) is a physical process that occurs in the interaction. However, it is significant that the principal mode in the mass signal is significantly higher than the principal mode in the shock position signal, and the subsequent low-frequency tones do not seem to be well correlated. This difference in time scales seems to be largely influenced by the high aspect ratio of the separation bubble in the present simulation. That is, h/δ_0 in the present simulation is approximately 68 % smaller than the height of the bubble in the 8° experiment considered by Piponniau *et al.* (2009), and as predicted by (3.10), the smaller bubble should result in a higher frequency of mass recovery in the bubble. (Recall that the discrepancy in separation bubble size with respect to experiment was discussed in § 3.1 and found to be a characteristic largely endemic to high-fidelity simulations with periodic spanwise boundary conditions.) On the other hand, it is possible that the scaling arguments made by Piponniau *et al.* (2009) could still be valid even if the mass entrainment model is not the principal force driving the low-frequency unsteadiness; that is, if the low-frequency tone number in the x_{shk} signal were normalized by the functions $\Phi(M_c)$ and $g(r, s)$, as suggested by Piponniau *et al.* (2009), one might expect the data to collapse to a value between approximately 5 and 9. Indeed, if we normalize the Strouhal number based on interaction length scale in this way, $St_L[\Phi(M_c)g(r, s)]^{-1} = 4.28$, which given the amount of scatter in the data, is in reasonable agreement with figure 12 in Piponniau *et al.* (2009). However, two facts remain which may suggest that the mass entrainment process is not the only mechanism forcing low-frequency motion of the reflected shock. First, as previously noted, the maximal frequency associated with mass in the separation bubble in the present simulation is higher than the frequency associated with shock motion; and secondly, there appear to exist additional low-frequency peaks in the shock motion signal for which there are no significant counterparts in the mass signal (e.g. $St = 0.024$ and 0.014). Thus, it is worthwhile considering the potential role other proposed mechanisms may play in the low-frequency unsteadiness, while allowing for the possibility of multiple first-order sources of forcing.

The acoustic resonance mechanism proposed by Pirozzoli & Grasso (2006) is considered next. As with the mass entrainment model, the acoustic resonance mechanism is initiated by vortices shed from the separation point. As Pirozzoli & Grasso (2006) hypothesize, these vortices then interact with the impinging shock foot, which results in the upstream propagation of slow-moving acoustic waves. Multiple pressure waves may then create a resonance with constructive interference and affect the position of the reflected shock foot. With the proposed mechanism as a starting point, Pirozzoli & Grasso (2006) then note that for resonance to occur, the shedding process and the acoustic radiation must share a common characteristic frequency,
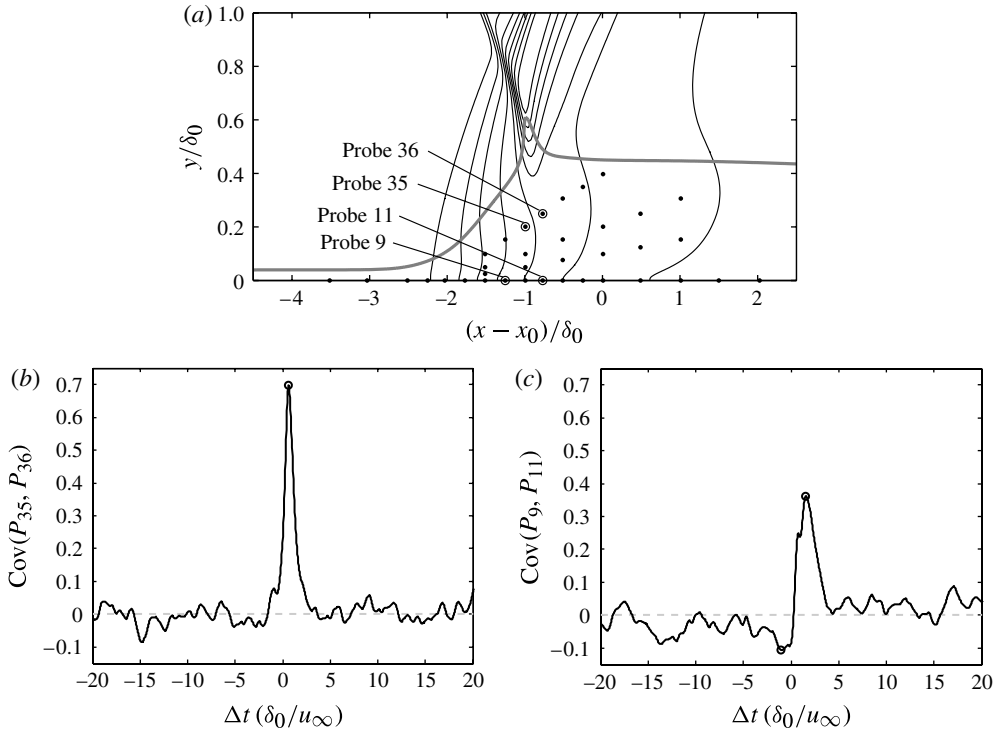
FIGURE 24. Determination of acoustic wave propagation speeds at various locations in the interaction. (*a*) Pressure probe locations are indicated by black dots. Thin black lines are ten evenly spaced contours of pressure between $\bar{p}/p_\infty = 1$ and 2.8. The thick grey line indicates the mean location of the sonic line. (*b*) Temporal covariance function computed for the pressure signal at probes 35 and 36. (*c*) Temporal covariance function computed for the pressure signal at probes 9 and 11.

which is described by

$$St_n = \frac{f_n \delta_0}{u_\infty} = \frac{\delta_0}{L^*} \frac{n - \alpha}{\dfrac{1}{\kappa} + \dfrac{M_\infty}{\gamma}}. \tag{3.11}$$

Here, L^* indicates the distance between the mean separation point and the mean location of the impinging shock foot (indicated by the streamwise location of the maximal height of the mean sonic line). Additionally, $\kappa = U_c/u_\infty$ and $\gamma = c^-/c_\infty$, where c_∞ indicates the free stream speed of sound, U_c indicates the downstream vortex convective velocity, c^- indicates the upstream speed of acoustic propagation, and α is an undetermined constant between 0 and 1 associated with the time delay between shock/vortex interaction and generation of the pressure wave.

In order to determine the values of κ and γ, we perform the same procedure originally used by Pirozzoli & Grasso (2006). As illustrated in figure 24, pressure signals at various probe locations throughout the interaction are extracted. Since the physical spacing of probe locations is known, it is straightforward to compute the velocities U_c and c^- if the time delay between probe locations can be reasonably determined. To determine this time delay, peaks in the temporal covariance of pressure

signals are analysed at various probe locations. First, to determine the downstream convective velocity U_c, probe locations 35 and 36 are selected, which are generally located along the trajectory of vortical structures shed from the separation point. The covariance of pressure signals from these two probes (illustrated in figure 24) demonstrates a significant positive correlation at positive Δt (indicating, as expected, that the downstream probe signal lags the upstream signal); by extracting this time delay, the first constant is computed to be $\kappa = 0.359$, which is slightly higher than the value of 0.27 originally computed by Pirozzoli & Grasso (2006) for an interaction at similar flow conditions. Next, to determine the upstream acoustic propagation velocity c^-, we follow the procedure used by Pirozzoli & Grasso (2006) and consider probe locations 9 and 11 along the wall in the separated flow region. The covariance of the pressure signals from these two probes (also illustrated in figure 24) demonstrates a weak but identifiable peak at negative time delay; by extracting this time delay, the second constant is computed to be $\gamma = 1.05$. This value, however, is quite a bit higher than the value $\gamma = 0.62$ originally reported by Pirozzoli & Grasso (2006). It should be noted, however, that the value of γ is particularly sensitive to the upstream time delay, which itself is particularly sensitive to under-sampling in the covariance of the probe data. Therefore, it is not unexpected that there should be significant uncertainty in determining the value of γ. Additionally, it is notable that the value 1.05 is much closer to the mean speed of sound ($\bar{c}/c_\infty$) at this location near the wall. Utilizing the values computed for κ and γ extracted from the LES data, and leaving α undetermined, the following frequencies are computed for the first five tones:

$$0.000 \leqslant St_1 \leqslant 0.207, \tag{3.12a}$$

$$0.207 \leqslant St_2 \leqslant 0.414, \tag{3.12b}$$

$$0.414 \leqslant St_3 \leqslant 0.622, \tag{3.12c}$$

$$0.622 \leqslant St_4 \leqslant 0.829, \tag{3.12d}$$

$$0.829 \leqslant St_5 \leqslant 1.036. \tag{3.12e}$$

The frequencies given in (3.12) are approximately 80 % greater than the frequencies predicted by Pirozzoli & Grasso (2006) for a similar interaction, a fact which reflects the practical difficulties of obtaining accurate values for U_c and c^-. In figure 25, however, the energy spectrum of the pressure signal at probe 9 is plotted, with the frequencies predicted both by the present work and by the original analysis by Pirozzoli & Grasso (2006). It is notable that the total time history available in the present analysis is $\sim$20 times longer than what was available to Pirozzoli & Grasso (2006). Although tempering our analysis with this understanding, the results of figure 25 raise several important issues. First, it is clear that the uncertainty in γ can lead to significant differences in the ranges predicted. However, regardless of whether the original ranges or the presently computed ranges are considered, the existence of significant peaks in the predicted intervals is found to be, at best, inconclusive (as illustrated in figure 25). While it does seem that there is at least one peak in most of the predicted intervals, the width of the intervals, as a result of the unknown parameter α, makes it very dubious that these peaks can be definitively linked with a specific acoustic resonance. Additionally, there are many intervals, including the interval of lowest frequencies, which contain multiple peaks – a phenomenon which would not be consistent with the model described by Pirozzoli & Grasso (2006). Therefore, we must conclude the following; first, if the acoustic mechanism described by Pirozzoli & Grasso (2006) exists in the system, then it is almost certainly not the only source of low-frequency forcing. Secondly, if the acoustic resonance mechanism exists in the
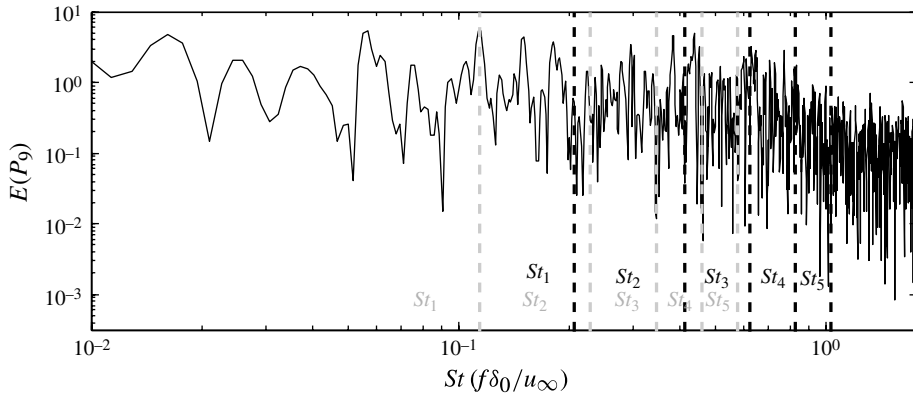
FIGURE 25. Energy spectrum of the pressure signal from probe 9 normalized to integrate to unity. Regions corresponding to the location of predicted resonance peaks are indicated by dashed lines. Frequencies given in (3.12) are overlaid in black, while frequencies predicted by Pirozzoli & Grasso (2006) are overlaid in grey.
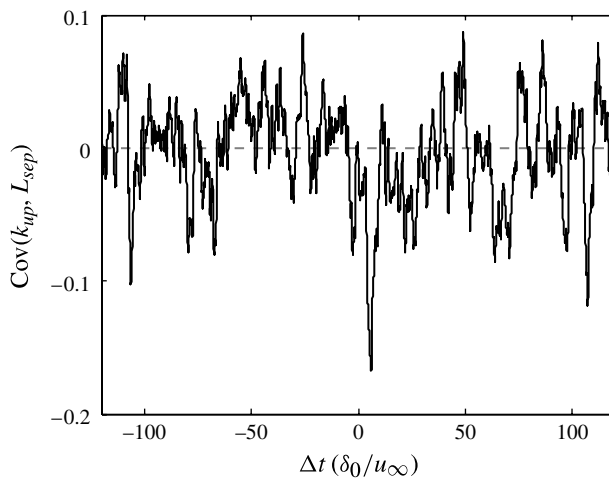

FIGURE 26. Temporal covariance function between k_{up}, the maximum TKE in the upstream boundary layer at $(x - x_0)/\delta_0 = -3.5$, and the length of separation, L_{sep}.

system, then the simplified model originally described by Pirozzoli & Grasso (2006) is not adequate to rigorously describe the low-frequency motion of the system until the parameter α can be closed.

Of course, an alternative hypothesis regarding the mechanism responsible for the low-frequency unsteadiness holds that forcing in the upstream boundary layer, rather than dynamics in the interaction itself, may be the underlying cause. Indeed, by investigating the temporal covariance of TKE in the undisturbed boundary layer with the separation length, as in figure 26, one can see that there exists a weak, albeit observable, negative correlation with a positive time delay of $\sim 6 \ \delta_0/u_\infty$. This correlation should make intuitive sense, as it says that the separation is more likely to be small when the incoming boundary layer is more energized (and thus more
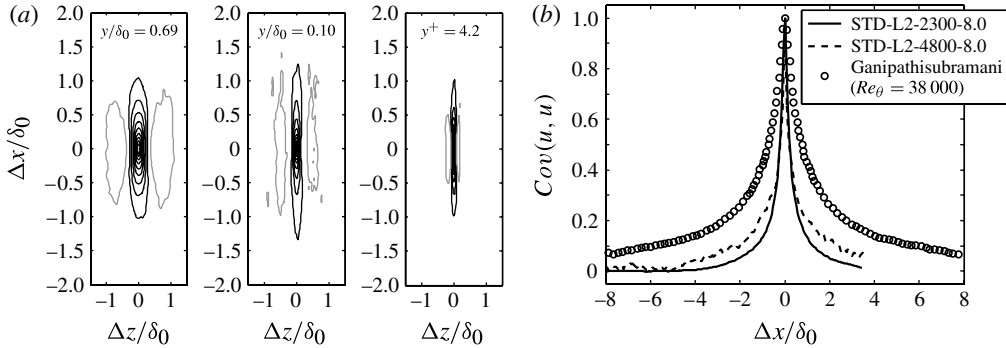
FIGURE 27. Assessment of coherence in the undisturbed boundary layer. (*a*) Contours of the two-point streamwise velocity correlation function (Cov(*u*, *u*)) at $y/\delta_0 = 0.686$ ($y^+ = 320$), $y/\delta_0 = 0.098$ ($y^+ = 45.7$), and $y/\delta_0 = 9.04 \times 10^{-3}$ ($y^+ = 4.21$). Black contours range from 0.1 to 1 in increments of 0.1, and the grey contour indicates the -0.05 contour. (*b*) A comparison of streamwise velocity correlation function across Reynolds numbers. Present data are taken at height $y/\delta_0 = 0.098$, while experimental data from Ganapathisubramani *et al.* (2006) are taken at height $y/\delta_0 = 0.16$.

resistant to separation); additionally, since the separation signal lags the upstream TKE signal, one may infer that the former is a consequence of the latter. This observation, however, is just a hint that upstream boundary layer characteristics may play a role in the low-frequency dynamics of the interaction. Ganapathisubramani, Clemens & Dolling (2006, 2007) and Ganapathisubramani *et al.* (2009) were the first to identify the effect that long, coherent structures in the upstream boundary layer could play in the low-frequency dynamics of their experimental compression corner geometry at $Re_\theta \approx 38\,000$. They found that coherent structures with length scales greater than $30\delta_0$ existed in their boundary layer and that significant correlation could be observed between these structures and the reflected shock position at time scales of the order of the low-frequency motions. This result prompted Ganapathisubramani *et al.* (2009) to conclude that the low-frequency oscillations were a result of forcing from so-called *superstructures* in the upstream boundary layer. We, therefore, intend to assess the superstructure hypothesis in regard to the present simulations by performing the same types of analysis used by Ganapathisubramani *et al.* (2009). For this analysis, it is necessary to consider instantaneous motions of the reflected shock in the spanwise plane; so, we therefore make use of a non-spanwise averaged database from the STD-L2-2300-8.0 simulation covering 2682 δ_0/u_∞ with snapshots taken every 0.32 δ_0/u_∞. Note that this database contains a longer time record than the previously utilized spanwise averaged database but with a greater delay between time slices.

The coherence of structures in the upstream boundary layer is first assessed, following the analysis of two-point velocity correlations utilized by Ganapathisubramani *et al.* (2006). In figure 27, contours are plotted of the spatial covariance of streamwise velocity at three different wall-normal heights. These correlations are computed at the recycling location in the undisturbed boundary layer mesh, which is injected as the inflow condition to the interaction (as described in § 2) at approximately $(x - x_0)/\delta_0 = -5.7$. It is notable that the qualitative arrangement of these contours is in good agreement with similar plots made for incompressible boundary layers by Kovasznay, Kibens & Blackwelder (1970), Ganapathisubramani *et al.* (2005) and Hutchins & Marusic (2007); that is, long streamwise coherence is

observed flanked on either side in the spanwise direction by regions of weak negative correlation. As Ganapathisubramani *et al.* (2005) point out, these outboard regions of negative correlation support the notion of adjacent low- and high-speed zones, which would be consistent with a hairpin vortex model. If a streamwise length scale λ_x^u is defined based on the 0.5 contour, it is found that λ_x^u at $y/\delta_0 = 0.10$ is equal to $0.427\delta_0$. By comparison, the same length scale computed by Ganapathisubramani *et al.* (2006) at $y/\delta_0 = 0.16$ was found to be $\sim 1.51\delta_0$. This difference is highlighted in figure 27(*b*). In this figure, covariance in the streamwise direction is plotted in order to compare directly with Ganapathisubramani *et al.* (2006); however, by additionally plotting the same covariance function from our higher-Reynolds-number simulation (STD-L2-4800-8.0), one begins to see what appears to be a trend of increasing length scale with increased Reynolds number. The scaling of λ_x^u with Reynolds number is not well understood (Ganapathisubramani *et al.* 2006); however, the majority of the available evidence seems to support the trend observed here. For instance, del Álamo *et al.* (2004) and Smits, McKeon & Marusic (2011) have pointed out how the streamwise velocity spectra tends to scale like the log of the Reynolds number, indicating that longer coherent structures are expected to be found with increasing turbulent Reynolds number. Similarly, Christensen *et al.* (2004) have found λ_x^u (defined in the same manner as we have done, based on the two-point velocity correlation) to increase with Reynolds number for experimental channel flows. Indeed, the length scale of the incompressible boundary layer described by Ganapathisubramani *et al.* (2005) at $Re_\theta = 2500$ was found to be four times smaller than the length scale of the compressible boundary layer at $Re_\theta = 38\,000$ described in Ganapathisubramani *et al.* (2006). It is notable, however, that Hutchins & Marusic (2007) found λ_x^u to collapse with scaling by δ_0 for some high-Reynolds-number incompressible boundary layers. In any case, it seems reasonable to conclude that at the relatively low Reynolds number of the present simulation, one should expect to see a reduction in streamwise length scale with respect to Ganapathisubramani *et al.* (2006).

Having established that the length scale of coherent streaks in the upstream boundary layer of the present simulation is $\sim 70\,\%$ shorter than that of the boundary layer ahead of the interaction in Ganapathisubramani *et al.* (2007, 2009), it is now desirable to identify what effect, if any, the coherent structures play on the low-frequency dynamics of the interaction. Following the same analysis utilized by Ganapathisubramani *et al.* (2007, 2009), correlations are computed between the location of initial separation, x_{sep}, and the line-averaged streamwise velocity, U_{line}, of the upstream boundary layer (that is, the streamwise velocity averaged in a constant wall-normal plane over a distance of approximately $5\delta_0$ ahead of the separation point, for a given spanwise location). In the work by Ganapathisubramani *et al.* (2007, 2009), particle image velocimetry (PIV) measurements were taken at a height of $0.2\delta_0$, which required them to utilize a *surrogate* function for separation; for them, separation was defined by any point such that $u(x, z) < \overline{U_{line}} - 4(\overline{U'_{line}U'_{line}})^{1/2}$, where it is assumed that the line-averaged velocity can be decomposed according to $U_{line} = \overline{U_{line}} + U'_{line}$. In the present simulations, data may be extracted much closer to the wall; thus, separation is presently defined based on the presence of reversed flow at a height of $y^+ = 4.21$. However, to assess the role of the surrogate, data are additionally considered in the plane of $y/\delta_0 = 0.1$, in which the location of separation, x_{sep}, is identified using the previously described surrogate function.

In figure 28(*a*), the joint probability density function (p.d.f.) between U'_{line} and x_{sep} at $\Delta t = 0$ is plotted. To construct this p.d.f., signal pairs are taken at each
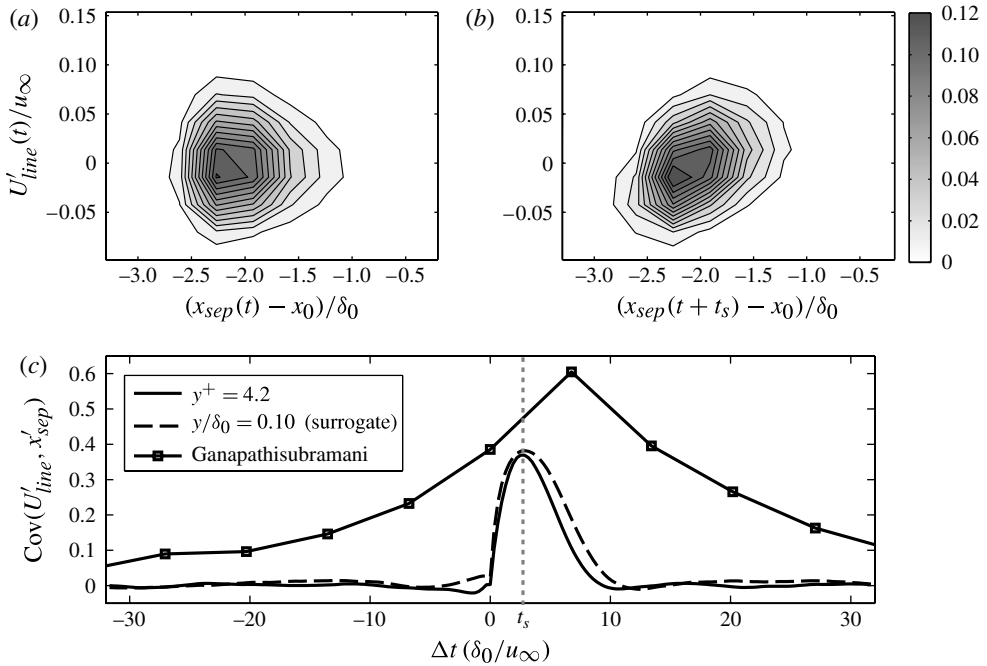
FIGURE 28. Assessment of the correlation between upstream coherent structures and low-frequency motions. (*a*) Joint p.d.f. between the U'_{line} and x'_{sep} normalized by the total number of samples. (*b*) Joint p.d.f. between U'_{line} and x_{sep} shifted by $\Delta t = t_s$, where t_s indicates the time of maximal correlation. (*c*) Temporal covariance function between the line-averaged streamwise velocity fluctuation ($U'_{line} = U_{line} - \overline{U_{line}}$) and the fluctuating component of the separation point ($x'_{sep} = x_{sep} - \overline{x_{sep}}$).

spanwise location for each time instant in the database for a total of 918 000 samples. Qualitatively, the joint p.d.f. looks very symmetric about $U'_{line} = 0$, which is indicative of little to no correlation between the two signals; indeed, the correlation coefficient is computed to be less than 0.01, which is in stark contrast to the coefficient of 0.4 computed by Ganapathisubramani *et al.* (2007). To assess the temporal correlation between the two signals, figure 28(*c*) plots the covariance function between U'_{line} and the fluctuating component of the x_{sep} signal. For comparison, figure 28(*b*) plots the joint p.d.f. that is obtained when the x_{sep} signal is shifted in time by $\Delta t = t_s$, the time of maximum correlation. Returning to the covariance plot, however, it is observed that regardless of the wall-normal height at which the covariance is computed, the result is very similar; this should provide further indication that the surrogate used by Ganapathisubramani *et al.* (2007, 2009) gives a good approximation of the true separation location. However, the covariance signal that is computed is qualitatively quite different from what was observed by Ganapathisubramani *et al.* (2009). First of all, the magnitude and location of the maximal peak is reduced with respect to Ganapathisubramani *et al.* (2009), and the correlation in the present simulation is seen to be strictly on the side of positive time delay. While this relationship makes intuitive sense (that is, the separation location strictly lags the upstream velocity signal), it is in contrast to Ganapathisubramani *et al.* (2009), who observed the tails of their signal extend into the negative time delay regime up to $\Delta t \approx -30\delta_0/u_\infty$.

Most importantly, however, the bandwidth of the correlation in the present simulation is significantly diminished with respect to the results of Ganapathisubramani *et al.* (2009). This indicates that time scales over which coherent structures in the incoming boundary layer may act on the separation appears to be limited to no longer than $\sim 10 \; \delta_0/u_\infty$. From this observation, we must conclude that the low-frequency motions previously described at Strouhal numbers between 0.05–0.01 (illustrated in figures 20 and 23) may not be attributed to forcing by superstructures alone. It should be noted, however, that this observation is limited to the present range of Reynolds numbers and is not expected to be applicable at higher Reynolds numbers, where the effect of superstructures may be more pronounced.

Three potential mechanisms have now been considered that each seek to explain the low-frequency unsteadiness by various cause-and-effect relationships, and in each case the results have largely been inconclusive insofar as no single mechanism could be determined to be the unique cause of the low-frequency motions. Indeed, a collection of evidence has been presented, some supporting and others in contradiction to each potential mechanism considered. It seems likely, therefore, that there may be multiple first-order effects, coupled and indistinguishable from one another, responsible for the low-frequency unsteadiness in the present flow regime.

3.3. *Assessment of RANS models*

Having completed our analysis of the flow physics of OSTBLI in §§ 3.1 and 3.2, we now seek to address uncertainties that may arise in the simulation of OSTBLI with lower-fidelity RANS models. Such uncertainties may lead to a systematic bias in RANS results in simulations of shock-induced separated flows. Pirozzoli *et al.* (2009), for instance, have compared LES and RANS simulations of OSTBLI ($M_\infty = 1.7$, $\phi = 6.0°$) at reduced Reynolds numbers similar to those considered in the present study; they found that their RANS solution, using the Spalart–Allmaras model (Spalart & Allmaras 1994), over-predicted separation length with respect to LES by as much as 100 %. In the present work, results using the two-equation Wilcox k–ω model (Wilcox 2006) are compared with LES results and with results obtained from the stress-ω model (Wilcox 2006), which is a Reynolds stress transport (RST) model that uses the specific-dissipation rate (ω) to provide turbulence scales. Standard stress limiters are utilized in the k–ω model, which are meant to reduce eddy viscosity in regions of high strain rate. In the present section, the basic assumptions made in these models are analysed and, using the LES database as a *surrogate-truth model*, the validity of those assumptions is addressed. For RANS results presented in this section, calculations were performed using the same flow conditions and grid cross-section as the LES results to which they are compared. In particular, RANS results are obtained at L2 grid resolution for wedge angles 6.5, 8.0 and 9.5° at $Re_\theta = 1500$, and results are also obtained at L4 grid resolution for an 8.0° wedge angle at $Re_\theta = 2300$ and 4800.

To begin, figure 29 compares some mean flow characteristics captured by the LES and RANS models. One feature common among the RANS models at $Re_\theta = 1500$ and 2300 is the consistent over-prediction of separation in the interaction. Though not shown here, at $Re_\theta = 4800$, the RST-based RANS results showed a slight under-prediction of the separation region. Overall, the RST model was seen to offer better predictions than the k–ω model. By considering the pressure traces plotted in figure 29(*a–c*), it is observed that even when the RANS solution provides a fairly accurate solution of shock penetration depth and pressure field in the outer boundary layer (e.g. the RST solution), the near-wall interaction may still be mis-predicted.
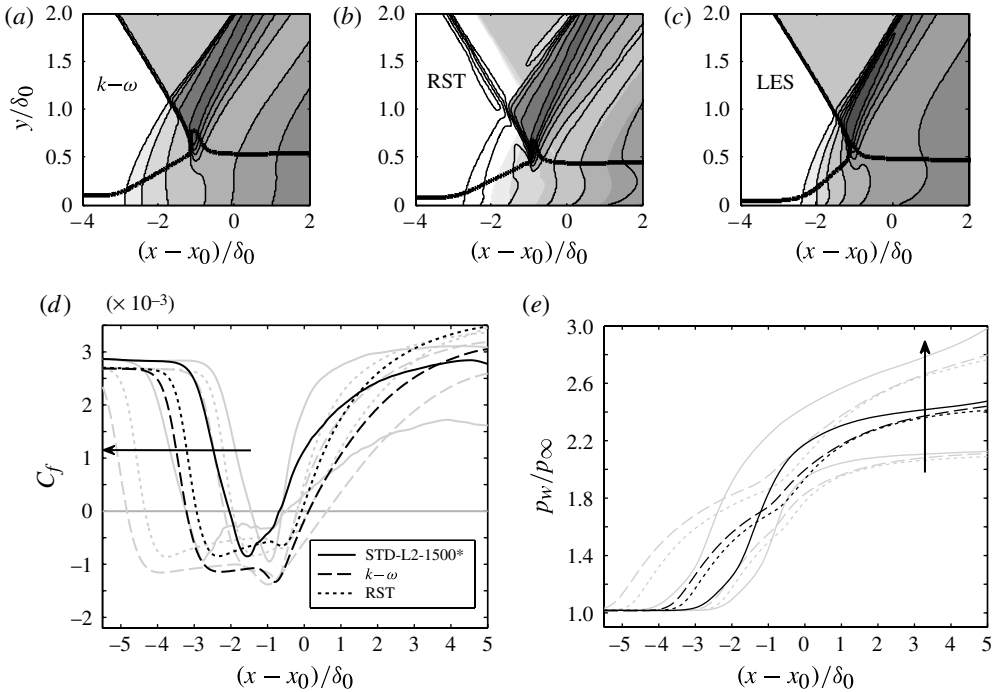
FIGURE 29. Comparison between LES and RANS simulations. (*a–c*) Ten evenly spaced contour levels are plotted between $\bar{p}/p_\infty = 1$ and 2.8. Shock penetration depth is identified by plotting the sonic line in thick solid black. (*d,e*) profiles of skin friction (*d*) and wall pressure (*e*) are additionally compared across three wedge angles. 8.0° results are highlighted in black, while 6.5 and 9.5° are shown in grey. Arrows indicate direction of increasing wedge angle.

The k–ω model exploits an analogy between turbulent and molecular mixing to model the Reynolds stress tensor, R_{ij}, by assuming it is proportional to the strain-rate tensor, S_{ij}, through an isotropic eddy viscosity that is held constant for each component of R_{ij}. Even though the RST model uses a fundamentally different closure which is capable of improved representations of the anisotropy properties of turbulence, both models exhibit the same propensity to over-predict separation (at $Re_\theta = 1500$). Utilizing the LES database, it is possible to dissect the predictive capability of these models. To begin, consider in figure 30 profiles of mean TKE and normal stress components of the Reynolds stress tensor obtained from LES and from the RANS models. From this figure, it is clear that the RANS models under-predict the R_{11} component while over-predicting the R_{22} component, a result which is consistent with previous work by DeBonis *et al.* (2012). In particular, the LES R_{11} component is found to be as much as five times larger than the LES R_{22} component. However, in the RANS, the R_{22} component and the R_{11} component are much closer in value. As a result, the TKE predicted by the RANS solutions more closely resembles the R_{22} component, whereas in the LES solution, TKE is dominated by R_{11}. While the RST results offer some improvement over the k–ω results, it is clear that there remains a qualitative difference in the shape of the Reynolds stress distributions with respect to LES. The use of viscous near-wall corrections to the RST models, as suggested in Wilcox (2006), was seen to improve the prediction of the stress anisotropy
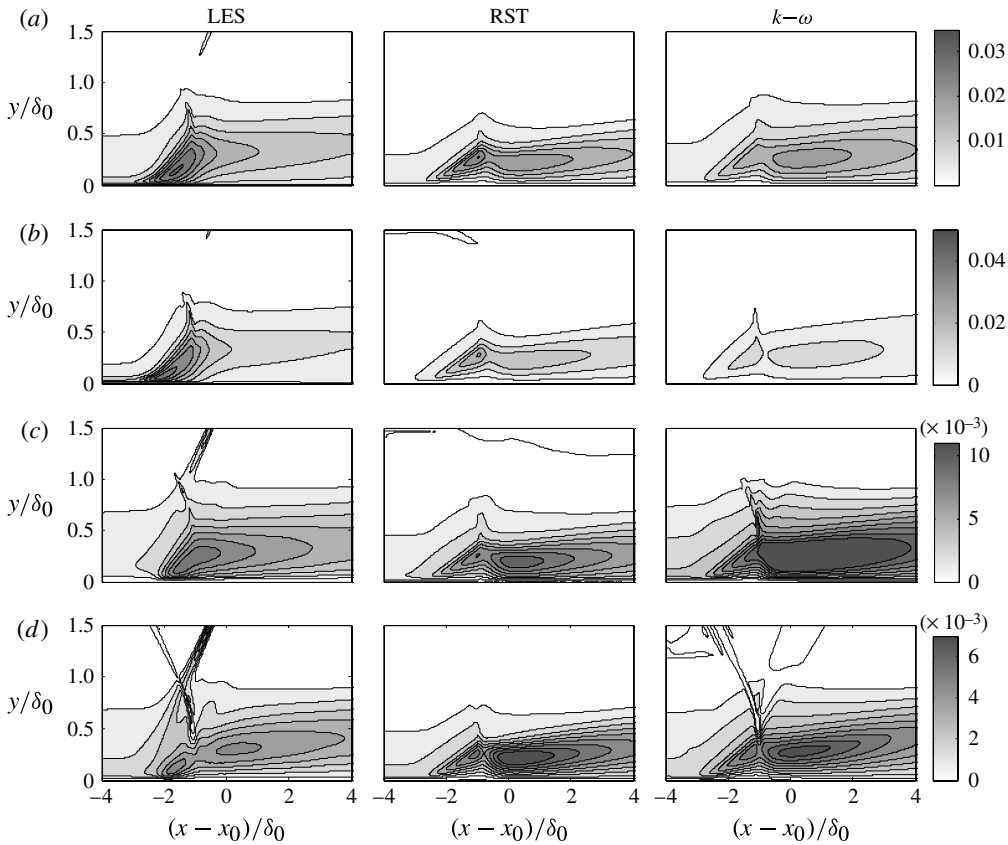
FIGURE 30. Contours of turbulence statistics are compared between LES and RANS. (*a*) Ten evenly spaced contours of TKE between $k/u_\infty^2 = 0$ and 0.035. (*b*) Ten evenly spaced contours of $\overline{u'u'}/u_\infty^2$ between 0 and 0.05. (*c*) Ten evenly spaced contours of $\overline{v'v'}/u_\infty^2$ between 0 and 0.011. (*d*) Ten evenly spaced contours of $-\overline{u'v'}/u_\infty^2$ between 0 and 0.007.

for $y/\delta_o < 0.1$, but did not improve the predictions of the extent of separation or the skin friction.

To probe further into the reason for the apparent discrepancies in turbulence quantities, our approach will be to consider how each method handles the transport of TKE and the Reynolds stresses. Figure 31 plots contours of the TKE budget terms computed using the three models. In this case, the LES balance has been given previously by (2.1), while the governing equation in RANS, in this case, is given by

$$
\frac{\partial}{\partial t}(\overline{\rho}k) = \underbrace{-\frac{\partial}{\partial x_j}\left(\overline{\rho}\tilde{u}_j k\right)}_{C_k^{RANS}} + \underbrace{R_{ij}\frac{\partial \tilde{u}_i}{\partial x_j}}_{P_k^{RANS}} - \underbrace{0.09\overline{\rho}k\omega}_{D_k^{RANS}} + \underbrace{\frac{\partial}{\partial x_j}\left(\mu\frac{\partial k}{\partial x_j}\right)}_{V_k^{RANS}} + \underbrace{\frac{\partial}{\partial x_j}\left(0.6\frac{\overline{\rho}k}{\omega}\frac{\partial k}{\partial x_j}\right)}_{T_k^{RANS}}.
$$

$$(3.13)$$

Notice that the compressibility term, K_k, is neglected in this formulation.

Although we see in figure 31 that the RST model provides significant improvement in prediction of production and dissipation over the simpler k–ω model, it is notable
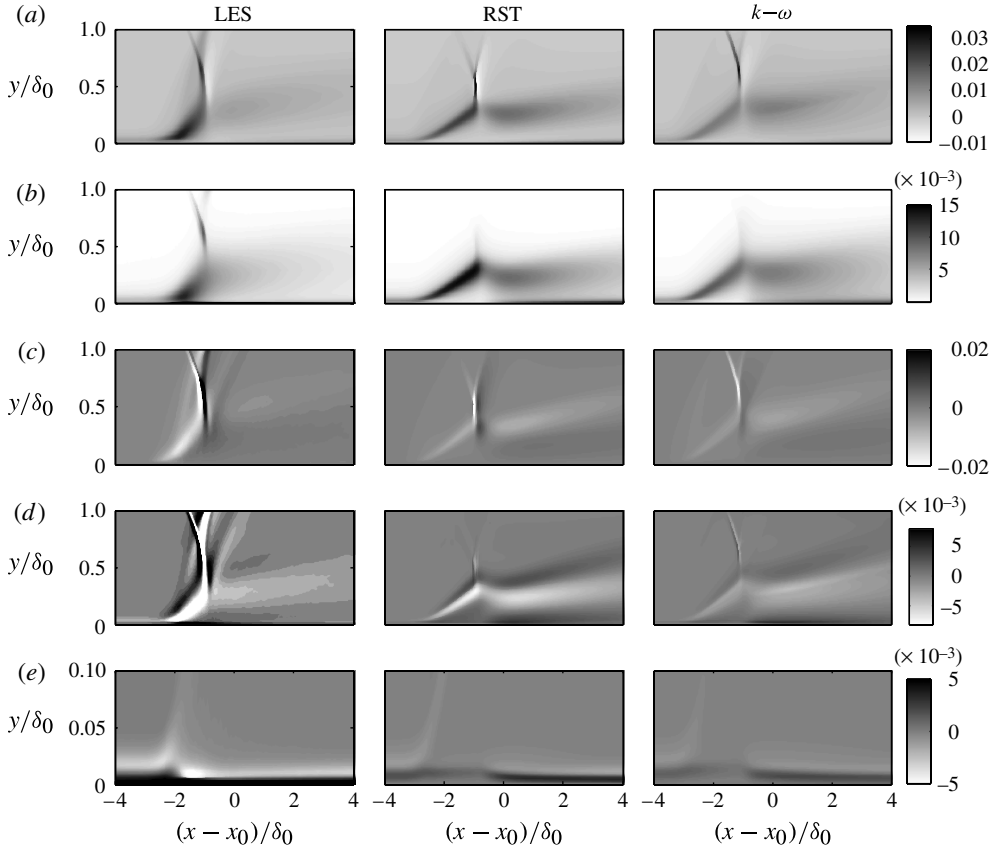
FIGURE 31. Contours of TKE budget terms are compared between LES and RANS. (*a*) Contours of production term, P_k. (*b*) Contours of dissipation term, D_k. (*c*) Contours of convective term, C_k. (*d*) Contours of turbulent transport term, T_k. (*e*) Contours of viscous diffusion term, V_k. Note that the vertical axis is reduced in (*e*) from $y/\delta_0 = 0.0$ to 0.1.

that both RANS models severely mis-predict near-wall behaviour and transport quantities in the shear layer. Specifically, mean convection and turbulent transport terms are grossly under-predicted. These observations are further quantified by considering traces of the TKE transport terms at two streamwise locations in figure 31. Upstream of the interaction in the undisturbed boundary layer, both RANS models are shown to provide good estimates of maximum production and dissipation, although the simple model of dissipation is asymptotically incorrect at the wall. In the LES, the viscous diffusion term largely balances dissipation at the wall, and an undershoot in viscous diffusion is apparently balanced by turbulent transport. In the RANS formulations however, the effects of viscous diffusion and turbulent transport are apparently much weaker. At the downstream location, the LES budget illustrates further the shortcomings of the RANS models. At this station, we observe that the production term is much larger than dissipation. Indeed, turbulent transport and convection seem to play nearly as large a role in balancing the production as dissipation. The RANS models, on the other hand, are limited in their ability to capture this phenomenon and thus under-predict production while simultaneously predicting qualitatively different profiles for turbulent transport.
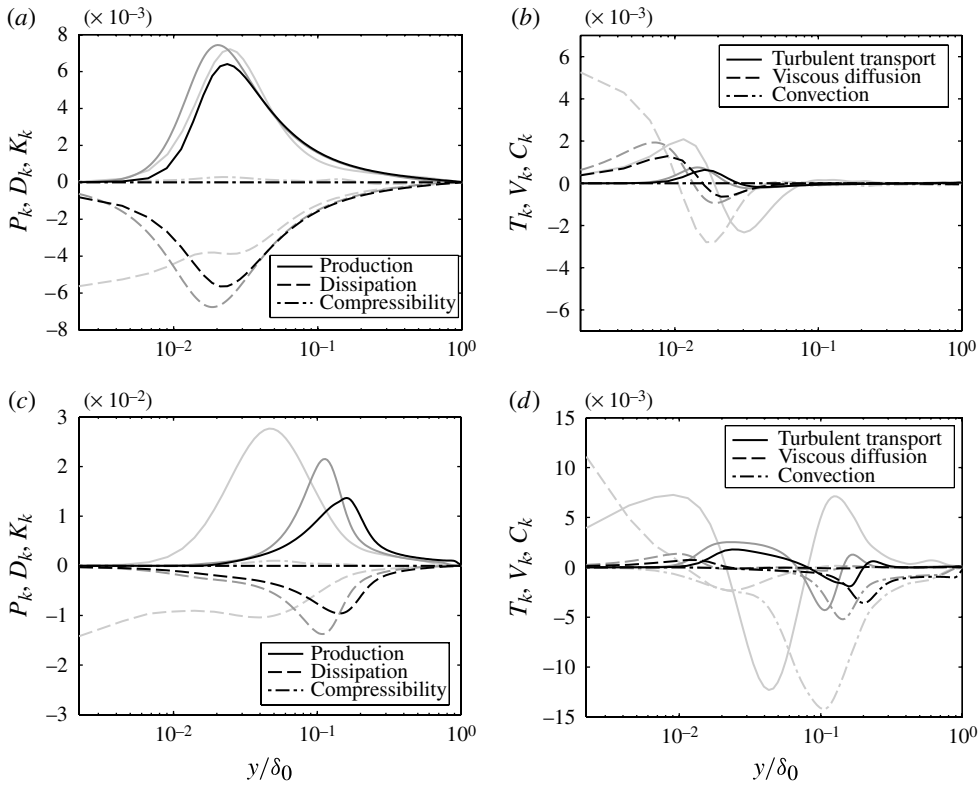
FIGURE 32. Comparison of TKE budget at two streamwise locations: (a,b) $(x - x_0)/\delta_0 = -4.5$ (upstream of interaction); (c,d) $(x-x_0)/\delta_0 = -2.0$ (within interaction). Light grey, LES; dark grey, RST; black, k–ω.

With the RST model, we can additionally compare transport of the individual Reynolds stress components. In the general sense, the transport equation for the Reynolds stress tensor, R_{ij}, is given by (Morrison 1992)

$$\frac{\partial R_{ij}}{\partial t} = C_{ij} + P_{ij} + \Pi_{ij} + M_{ij} + V_{ij} + T_{ij} + D_{ij}. \tag{3.14}$$

Here, C_{ij}, P_{ij}, Π_{ij}, M_{ij}, V_{ij}, T_{ij} and D_{ij} represent, respectively, terms due to convection, production, pressure-strain correlation, mass flux variation, viscous diffusion, turbulent transport, and dissipation. Explicitly, these terms are given by

$$C_{ij} = -\frac{\partial \tilde{u}_k R_{ij}}{\partial x_k}, \quad P_{ij} = -R_{ik}\frac{\partial \tilde{u}_j}{\partial x_k} - R_{jk}\frac{\partial \tilde{u}_i}{\partial x_k}, \quad \Pi_{ij} = \overline{p'\frac{\partial u_i'}{\partial x_j}} + \overline{p'\frac{\partial u_j'}{\partial x_i}}, \tag{3.15}$$

$$M_{ij} = \overline{u_i''}\left(\frac{\partial \overline{\sigma}_{jk}}{\partial x_k} + \frac{\partial \overline{\sigma}_{ik}}{\partial x_k} - \frac{\partial \overline{p}}{\partial x_j} - \frac{\partial \overline{p}}{\partial x_i}\right), \quad V_{ij} = \frac{\partial \overline{\sigma_{ik}' u_j' + \sigma_{jk}' u_i'}}{\partial x_k}, \tag{3.16}$$

$$T_{ij} = -\frac{\partial\left[\overline{\rho u_i'' u_j'' u_k''} + \left(\overline{p' u_i'}\delta_{jk} + \overline{p' u_j'}\delta_{ik}\right)\right]}{\partial x_k}, \quad D_{ij} = \overline{\sigma_{ik}'\frac{\partial u_j'}{\partial x_k}} + \overline{\sigma_{jk}'\frac{\partial u_i'}{\partial x_k}}. \tag{3.17}$$

Figure 33 plots contours of a few of the most significant contributors to the R_{11} budget from both LES and the RST RANS model. From these plots, we see that the
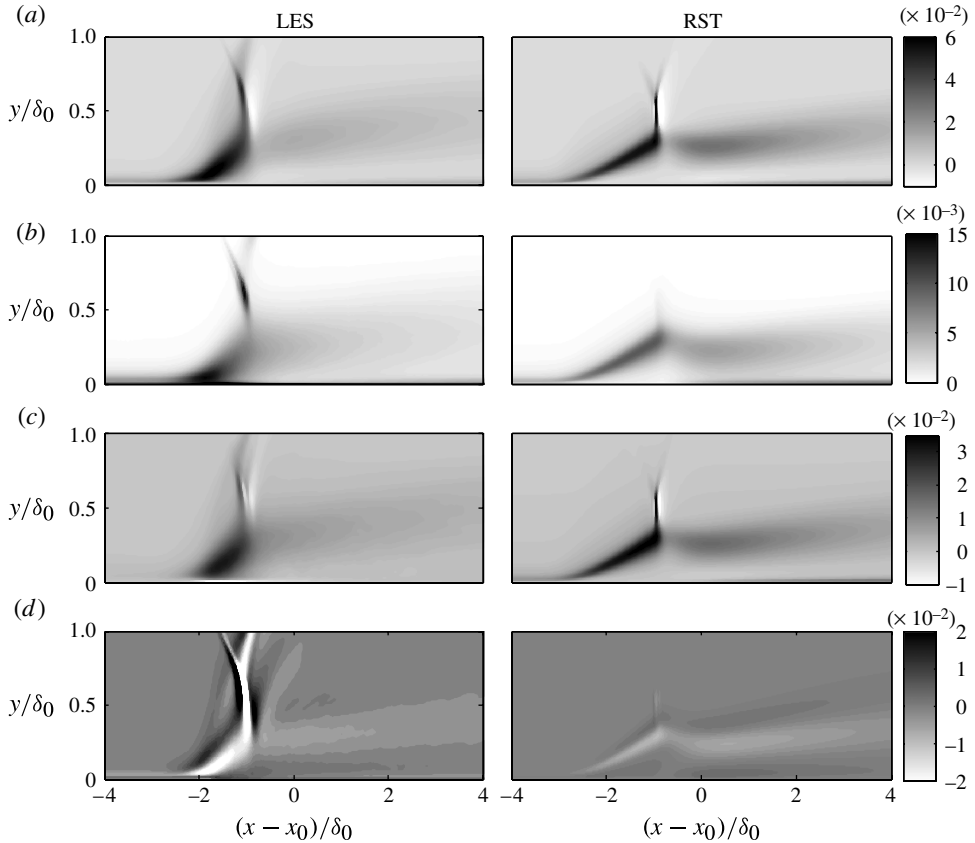
FIGURE 33. Contours of R_{11} budget terms are compared between LES and RST. (*a*) Contours of production term, P_{11}. (*b*) (Negated) contours of dissipation term, $-D_{11}$. (*c*) Contours of (negated) pressure-strain term, $-\Pi_{11}$. (*d*) Contours of turbulent transport term, T_{11}.

RST solution actually captures major trends and the general magnitude of production, dissipation, and pressure strain quite well. The effect of turbulent transport, however, is severely under-predicted by the RST solution. In figure 34, the same terms are plotted for the R_{22} transport budget. In this case, the LES production term P_{22} demonstrates a qualitatively different profile as compared with P_{11}; however, this anisotropy is not captured by the RST results. These observations are further quantified in figure 35, which plots traces of the production, dissipation, pressure-strain, and turbulent transport terms at two locations in the flow. At the upstream location in the undisturbed boundary layer, we see that the LES P_{11} production is matched well by the RST results. Within the interaction, the RST results seem to somewhat under-predict the dissipation and over-predict the pressure-strain correlation, but in general there is considerable agreement with LES. The R_{22} budget predicted by RST, however, differs from LES. In particular, in the LES, it is observed that pressure strain is approximately balanced by turbulent transport in the near-wall region. Also, the assumption of isotropic dissipation (i.e. $\epsilon_{ij} = (2/3)0.09\rho k\omega\delta_{ij}$) is shown to be poor, as seen from the comparison of the dissipation terms in the R_{11} and R_{22} budgets. It is, however, interesting to note that the pressure-strain correlation, which is based on the
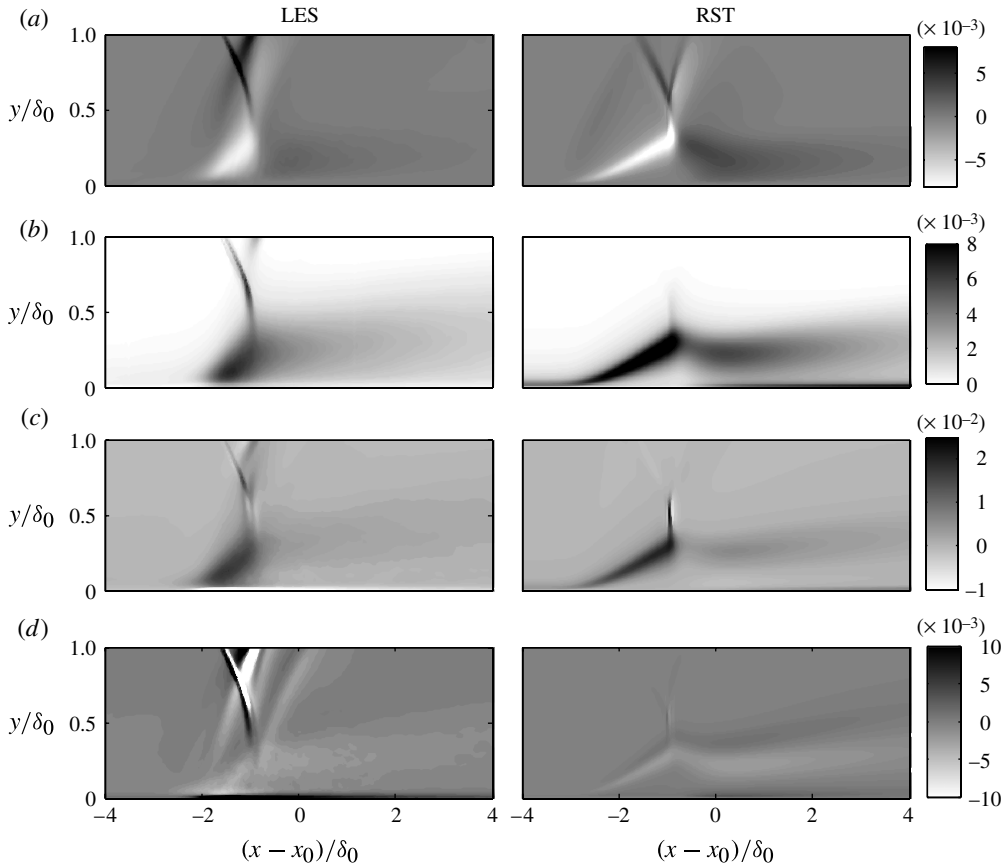
FIGURE 34. Contours of R_{22} budget terms are compared between LES and RST. (*a*) Contours of production term, P_{22}. (*b*) (Negated) contours of dissipation term, $-D_{22}$. (*c*) Contours of pressure-strain term, Π_{22}. (*d*) Contours of turbulent transport term, T_{22}.

rather simple LRR formulation (Launder, Reece & Rodi 1975) is well represented in both budgets. As discussed previously, the RST does not correctly capture the effects of turbulent transport, instead predicting that pressure strain is balanced by negative production and dissipation.

In the context of Reynolds stress transport budgets, we have seen how qualitative differences in the shape of the production field in LES are not captured by the RANS simulations, suggesting that effects of anisotropy are being missed. Thus, to better visualize the effect of anisotropy in the Reynolds stress tensor, the barycentric mapping technique proposed by Banerjee *et al.* (2007) is utilized. This method uses a linear reconstruction of the anisotropy eigenvalues, rather than the nonlinear form proposed by Lumley & Newman (1977), to provide a non-distorted visual representation of the anisotropy invariant map. Equation (3.18) describes how the three barycentric coordinates, C_{ic}, are computed from the ordered eigenvalues (λ_i) of the Reynolds stress anisotropy tensor and how these coordinates are then mapped onto a triangle with vertices (x_{ic}, y_{ic}):
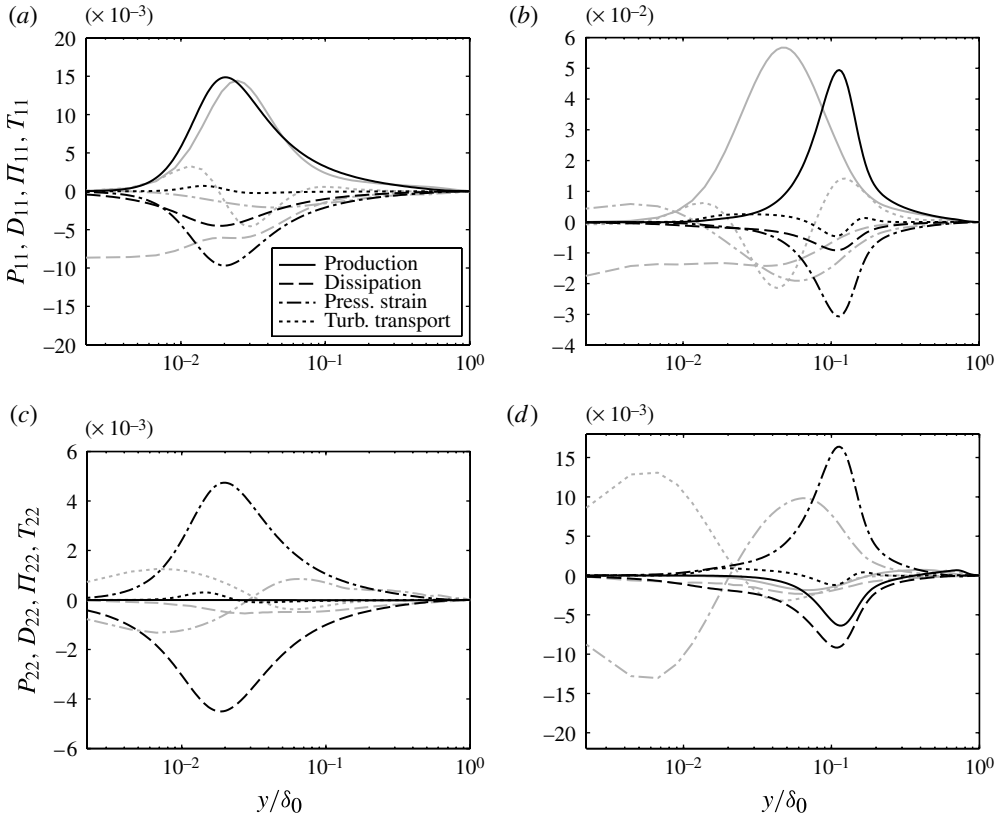
$$C_{1c} = \lambda_1 - \lambda_2, \tag{3.18a}$$

FIGURE 35. Comparison of R_{11} (a,b) and R_{22} (c,d) budgets at two streamwise locations: (a,c) $(x - x_0)/\delta_0 = -4.5$ (upstream of interaction); (b,d) $(x - x_0)/\delta_0 = -2.0$ (within interaction). Light grey, LES; black, RST.

$$C_{2c} = 2\,(\lambda_2 - \lambda_3)\,, \tag{3.18b}$$

$$C_{3c} = 3\lambda_3 + 1, \tag{3.18c}$$

$$x = C_{1c}x_{1c} + C_{2c}x_{2c} + C_{3c}x_{3c}, \tag{3.18d}$$

$$y = C_{1c}y_{1c} + C_{2c}y_{2c} + C_{3c}y_{3c}. \tag{3.18e}$$

Since the barycentric coordinates are linear in construction and since they sum to unity, it is possible to visualize the anisotropy of a flow field by interpreting the barycentric coordinates as a red-green-blue (RGB) colour value and generating an image from these values, as illustrated in figure 36. For this visualization, a map has been chosen such that C_{1c} is mapped to red, C_{2c} is mapped to green, and C_{3c} is mapped to blue. Thus, the flow field   visualization will appear more red, green, or blue to correspond to respective one-, two-, or three-component shifts in the local anisotropy tensor. By comparing flow field anisotropy in this way between the LES and RANS results, one is able to quickly identify some qualitative trends in the turbulence which are present in the LES but missing in the RANS. For instance, in figure 37, in which the RGB-coded anisotropy mapping is applied to the flow fields obtained using both LES and RANS, one can see how the RANS approaches miss the strongly one-component nature of the upstream boundary layer
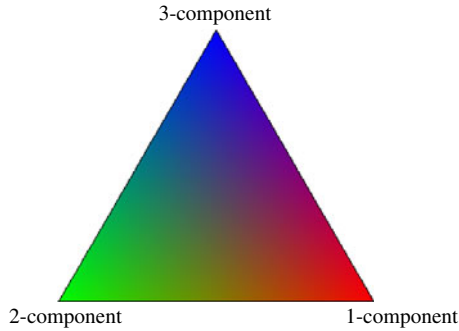
FIGURE 36. The barycentric anisotropy mapping technique. Invariants of the anisotropy tensor are mapped to a coordinate in the equilateral triangle and to a three-component RGB colour code.
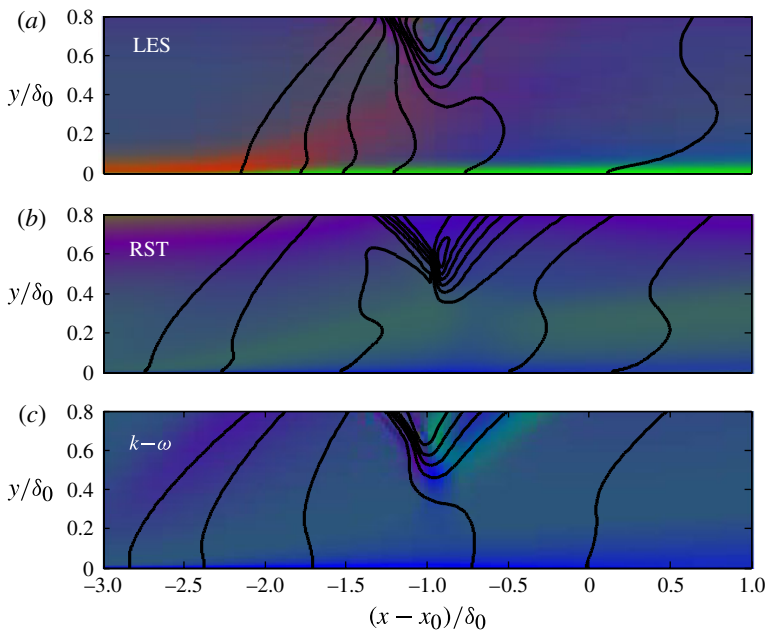
FIGURE 37. The barycentric anisotropy mapping technique applied to the OSTBLI problem solved with LES (*a*), RST (*b*), and *k*–*ω* (*c*). Interaction is coloured by RGB colour corresponding to the location of anisotropy invariants in the barycentric map illustrated in figure 36. Ten evenly spaced contours of pressure from p/p_∞ are overlaid in black.

near the wall. Additionally, it is clear in the LES that this one-component behaviour extends into the interaction as the boundary layer separates away from the wall. However, neither of the RANS solutions are able to capture this feature. Indeed it is likely that the failure of the RANS models to capture this feature is related to the previously discussed shortcomings of the RANS models to properly predict the effects of turbulent transport, especially in the shear layer. Similarly, it is observed in the LES

that the near-wall anisotropy in the recovering boundary layer demonstrates strong two-component behaviour, while the lower-fidelity solutions generally fail to capture this behaviour as well. Perhaps the most striking observation to be made from figure 37, however, is the similarity of the anisotropy fields in the two RANS approaches. This observation should suggest that it may not be enough to solve additional transport equations to fully capture the effects of anisotropy in the flow field.

4. Conclusions

In the present work, a numerical database of large-eddy simulations, covering a range of parametric variations, has been utilized to investigate the flow physics and modelling of oblique shock/turbulent boundary layer interaction. To establish confidence in baseline results, in §2.3, we first sought to describe the role of numerical dissipation in our calculations. Although it was found that the filtering operation introduced unwanted numerical dissipation, it was determined that grid resolution levels L2 and higher were sufficient to resolve TKE production, proving that the numerical dissipation due to filtering serves essentially as a subgrid model of dissipation without causing significant damage to the turbulence budgets. By then comparing TKE budget terms with available DNS data in §2.4, confidence was established in a baseline solution by demonstrating good agreement in both the upstream and interaction regions for all terms in the TKE budget.

In §3.1, trends have been extracted in mean flow characteristics and conservation budgets with respect to flow conditions (Reynolds number and shock strength) which may, in general, be uncertain. It was found, for instance, that the mean separation length scale was not heavily dependent on Reynolds number, over the range considered ($Re_\theta = 1500$–4800); this numerical result was found to be in agreement with experimental comparisons made by Souverein (2010) between interactions at $Re_\theta = 50\,000$ and $Re_\theta = 5100$. By varying the shock-generating wedge angle, it was observed how the increased shock strength associated with a change of as little as $1°$ could move an interaction from the incipient regime to fully separated. Analysis of the spectral content of these simulations demonstrated how increased shock strength could lead to more intense low-frequency oscillation at longer time scales, even when normalizing to account for the increased length of interaction. Additionally, since the results analysed in this manner were provided the same inflow turbulence (at different wedge angles), a preliminary indication was given that upstream dynamics in the boundary layer were probably not the primary driver of low-frequency unsteadiness, at least in the case of the strongest interactions. Attention was then turned to the effect of shock strength on the various terms in the momentum and turbulence kinetic energy budgets. For each equation, budget terms were plotted for the seven available wedge angles at streamwise stations upstream and downstream of the incident shock foot. In the streamwise momentum budget, it was observed that at the upstream station, the magnitude of budget terms tended to increase with increasing wedge angle, while downstream this trend was reversed. While somewhat counter-intuitive, this observation may be explained by the penetration depth of the incident shock, which extends deeper in the case of a weaker shock. In the wall-normal momentum budget, it was found that only contributions due to pressure gradient and turbulent transport are important in most of the boundary layer. By plotting the TKE budget terms, a trend of increasing magnitude upstream and decreasing magnitude downstream with increasing wedge angle was again observed.

Next, in §3.2, an evaluation has been made of several proposed mechanisms underlying the previously discussed low-frequency unsteady motion in the separation bubble and reflected shock position. First, the mass entrainment model proposed by Piponniau *et al.* (2009) was considered, which suggests that a deficit of mass in the separation bubble might require recovery on a long time scale, which could be responsible for the low-frequency unsteadiness. To assess the potential for this mechanism to exist in the present simulations, integrated mass and momentum budgets were computed on moving control volumes representing both the separation bubble and the greater interaction region. By computing the correlations between and comparing spectral content of the shock position and the integrated mass signal in the separation bubble, some evidence was found to suggest the two are related – specifically that the two are negatively correlated with a positive time delay, indicating that the reflected shock moves upstream as a result of increased mass in the separation bubble. Additionally, the predicted time frequency of the principal mode of the mass recovery (that is, the frequency with the greatest energy density) was found to be in excellent agreement with the frequency predicted analytically by Piponniau *et al.* (2009). However, the primary mode of the shock position signal was found to be somewhat lower, and it was observed that several additional low-frequency tones exist in the shock position signal which could not be accounted for from the integral mass signal alone. Therefore, it is likely that additional mechanisms contribute to the low-frequency forcing of the shock position. Following this reasoning, the acoustic resonance mechanism described by Pirozzoli & Grasso (2006) was considered next, which hypothesizes that upstream-propagating acoustic waves generated by shock/vortex interactions at the impinging shock foot could create a resonance with constructive interference that would influence the position of the reflected shock foot. Following the same procedure utilized by Pirozzoli & Grasso (2006), upstream and downstream speeds of acoustic propagation were extracted to determine the modes that would be visible if such a mechanism were to exist in our system. The ranges predicted, however, proved to be generally inconclusive, as each range was quite large, due to the existence of the unclosed parameter α; additionally, many ranges contained more than one peak, which would not be consistent with the proposed model. Thus, it is concluded that for the acoustic resonance model to be useful as a diagnostic tool, more work must be done to determine α, the time delay between shock/vortex interaction and the release of upstream-propagating pressure waves. To assess the potential effect of forcing due to structures in the incoming boundary layer, attention was next turned to the superstructure theory proposed by Ganapathisubramani *et al.* (2009), who identified a strong correlation between the existence of long, coherent structures in their experimental boundary layer at $Re_\theta = 38\,000$ and the position of the reflected shock in a compression corner interaction. Although some evidence is found in the present LES to indicate a correlation between upstream TKE and the position of the reflected shock, the length scale of structures in the incoming boundary layer is found to be much shorter than in the experiments by Ganapathisubramani *et al.* (2009). As a result, correlation between the location of separation and the upstream line-averaged velocity is found to extend only out to $\sim 10\delta_0/u_\infty$, which could not account for the low-frequency peaks observed as low as $St = 0.00853$. However, limited variation in Reynolds number did suggest a trend towards increasing length scale with increasing Reynolds number, which very likely could account for the discrepancy. We therefore conclude that forcing due to superstructures is not the cause of the lowest-frequency motions in the present simulations, although the effect of this type of forcing is expected to be much greater at higher Reynolds number.

Finally, in §3.3, we have sought to address the cause of modelling errors in representative eddy-viscosity and RST-based RANS solutions of OSTBLI. These results demonstrated a systematic bias towards over-prediction of the size of separation with respect to the LES in the low-Reynolds-number simulations. Further investigation revealed that the RANS models were misrepresenting, both qualitatively and quantitatively, the TKE due largely to the relative under-prediction of the R_{11} and over-prediction of the R_{22} normal components in the Reynolds stress tensor. To address this issue, contributions to the TKE and Reynolds stress transport equations were plotted, which indicated that the biggest discrepancy in the RANS models was due to a failure to account for the effects of turbulent transport in the shear layer. Overall, these results suggest that the RST model offers improved predictions as it is able to better represent some aspects of the turbulence anisotropy when compared to the eddy-viscosity model. Even though encouraging representations of the pressure-strain correlation are noted, the treatment of the turbulence transport term using a simple gradient diffusion hypothesis and the assumption of an isotropic dissipation rate are seen to limit the accuracy of the RST model. By utilizing the barycentric mapping technique described by Banerjee *et al.* (2007) and assigning an RGB colour value to each barycentric component of the transformed invariants of the anisotropy tensor, it was possible to visualize the two-dimensional anisotropy field in each simulation. These visualizations confirmed earlier observations that the mostly single-component turbulence from the near-wall region in the LES was extending into the interaction and that this feature is apparently missed by RANS, especially in the shear layer region.

Taken as a whole, the present work represents the culmination of a concerted effort to investigate a few of the lingering questions associated with the physics and simulation of OSTBLI. It is our belief that only through the better understanding and quantification of uncertainties can the flow physics community move towards improved confidence in lower-fidelity simulations involving shock-induced separation. For instance, by providing data identifying the effect of variation in inflow parameters, it is possible to identify regions that may be sensitive to aleatory uncertainties. Similarly, by providing information on the appropriateness of turbulence closures, it is possible to identify regions that may be sensitive to epistemic uncertainties; and, by better understanding the inherent unsteadiness, it may be possible to better predict and account for fluctuating pressure and thermal loads in the design of physical systems. The present work, therefore, represents an important step towards these goals in the understanding and mitigation of uncertainties in shock/boundary layer interactions.

Acknowledgements

Appendix

Tables 3 and 4 provide detailed flow conditions and grid data, respectively, for each of the 19 simulations computed.

Simulation	Re_θ	Re_{δ^*}	Re_δ	$H(\delta^*/\theta)$	C_f	u_τ/u_∞	Total time integration (δ_0/u_∞)
STD-L1-2300-8.0	2030	6922	25 836	3.41	2.31×10^{-3}	0.0423	1772
STD-L1-4800-8.0	4478	14 991	54 796	3.35	1.91×10^{-3}	0.0381	221
STD-L2-1500-6.5	1498	5133	17 598	3.43	2.90×10^{-3}	0.0479	1419
STD-L2-1500-7.0	1498	5133	17 598	3.43	2.90×10^{-3}	0.0479	1419
STD-L2-1500-7.5	1498	5133	17 598	3.43	2.90×10^{-3}	0.0479	1419
STD-L2-1500-8.0	1498	5133	17 598	3.43	2.90×10^{-3}	0.0479	1419
STD-L2-1500-8.5	1498	5133	17 598	3.43	2.90×10^{-3}	0.0479	1419
STD-L2-1500-9.0	1498	5133	17 598	3.43	2.90×10^{-3}	0.0479	1419
STD-L2-1500-9.5	1498	5133	17 598	3.43	2.90×10^{-3}	0.0479	1419
STD-L2-2300-8.0	2258	7672	26 014	3.40	2.60×10^{-3}	0.0450	2769
STD-L2-4800-8.0	4775	15 970	54 330	3.34	2.09×10^{-3}	0.0396	172
STD-L3-2300-6.5	2274	7776	26 084	3.42	2.59×10^{-3}	0.0450	401
STD-L3-2300-8.0	2281	7778	26 140	3.41	2.60×10^{-3}	0.0451	188
STD-L3-2300-9.5	2281	7756	26 399	3.40	2.60×10^{-3}	0.0453	103
STD-L4-2300-8.0	2295	7817	26 067	3.41	2.61×10^{-3}	0.0451	622
LONG-L2-1500-9.5	1491	5100	17 596	3.42	2.88×10^{-3}	0.0477	136
LONG-L2-2300-8.0	2271	7729	26 064	3.40	2.58×10^{-3}	0.0448	147
WIDE-L1-2300-8.0	2064	6957	26 377	3.37	2.33×10^{-3}	0.0429	383
WIDE-L2-2300-8.0	2271	7721	26 127	3.40	2.59×10^{-3}	0.0450	393
DNS[a]	2330	8320	29 000	3.60	2.51×10^{-3}	0.0493	92.8
Experiment[b]	5100	18 000	59 053	3.53	2.10×10^{-3}	—	—

TABLE 3. Characteristic properties of the undisturbed boundary layer. [a] Pirozzoli & Bernardini (2011), [b] Piponniau *et al.* (2009).

Simulation	N_x	N_y	N_z	Boundary layer mesh $\frac{L_x}{\delta_0}$	$\frac{L_y}{\delta_0}$	$\frac{L_z}{\delta_0}$	Δx^+	Δy^+	Δz^+	Points
STD-L1-2300-8.0	161	134	55	17.4	9.87	3.48	46	1–28	28	1.19M
STD-L1-4800-8.0	321	250	108	17.8	10.1	3.56	46	1–27	27	8.67M
STD-L2-1500-6.5	201	174	81	17.0	9.66	3.41	28	1–14	14	2.83M
STD-L2-1500-7.0	201	174	81	17.0	9.66	3.41	28	1–14	14	2.83M
STD-L2-1500-7.5	201	174	81	17.0	9.66	3.41	28	1–14	14	2.83M
STD-L2-1500-8.0	201	174	81	17.0	9.66	3.41	28	1–14	14	2.83M
STD-L2-1500-8.5	201	174	81	17.0	9.66	3.41	28	1–14	14	2.83M
STD-L2-1500-9.0	201	174	81	17.0	9.66	3.41	28	1–14	14	2.83M
STD-L2-1500-9.5	201	174	81	17.0	9.66	3.41	28	1–14	14	2.83M
STD-L2-2300-8.0	267	233	108	17.3	9.80	3.46	30	1–15	15	6.72M
STD-L2-4800-8.0	533	443	214	17.9	10.2	3.59	29	1–14	14	50.5M
STD-L3-2300-6.5	320	269	129	17.3	9.78	3.45	25	1–12	12	11.1M
STD-L3-2300-8.0	320	269	129	17.2	9.76	3.44	25	1–12	12	11.1M
STD-L3-2300-9.5	320	269	129	17.0	9.66	3.41	25	1–12	12	11.1M
STD-L4-2300-8.0	400	321	161	17.3	9.78	3.45	20	1–10	10	20.7M
LONG-L2-1500-9.5	201	184	81	17.0	13.6	3.41	28	1–14	14	3.00M
LONG-L2-2300-8.0	267	246	108	17.3	14.4	3.45	29	1–15	15	7.09M
WIDE-L1-2300-8.0	161	134	108	17.1	9.67	6.82	47	1–28	28	2.27M
WIDE-L2-2300-8.0	267	233	211	17.2	9.76	6.89	29	1–15	15	13.1M

TABLE 4. (Continued on next page)

Interaction mesh

Simulation	N_x	N_y	N_z	$\frac{L_x}{\delta_0}$	$\frac{L_y}{\delta_0}$	$\frac{L_z}{\delta_0}$	Δx^+	Δy^+	Δz^+	Points
STD-L1-2300-8.0	154	134	55	11.6	9.87	3.48	46–28–46	1–28	28	1.13M
STD-L1-4800-8.0	321	250	108	11.9	10.1	3.56	46–27–46	1–27	27	8.67M
STD-L2-1500-6.5	200	174	81	11.4	9.66	3.41	28–16–28	1–14	14	2.82M
STD-L2-1500-7.0	200	174	81	11.4	9.66	3.41	28–16–28	1–14	14	2.82M
STD-L2-1500-7.5	200	174	81	11.4	9.66	3.41	28–16–28	1–14	14	2.82M
STD-L2-1500-8.0	200	174	81	11.4	9.66	3.41	28–16–28	1–14	14	2.82M
STD-L2-1500-8.5	200	174	81	11.4	9.66	3.41	28–16–28	1–14	14	2.82M
STD-L2-1500-9.0	200	174	81	11.4	9.66	3.41	28–16–28	1–14	14	2.82M
STD-L2-1500-9.5	200	174	81	11.4	9.66	3.41	28–16–28	1–14	14	2.82M
STD-L2-2300-8.0	267	233	108	11.5	9.80	3.46	30–17–30	1–15	15	6.72M
STD-L2-4800-8.0	530	443	214	12.0	10.2	3.59	29–16–29	1–14	14	50.2M
STD-L3-2300-6.5	320	269	129	11.5	9.78	3.45	25–14–25	1–12	12	11.1M
STD-L3-2300-8.0	320	269	129	11.5	9.76	3.44	25–14–25	1–12	12	11.1M
STD-L3-2300-9.5	320	269	129	11.4	9.66	3.41	25–14–25	1–12	12	11.1M
STD-L4-2300-8.0	407	321	161	11.5	9.78	3.45	20–11–20	1–10	10	21.0M
LONG-L2-1500-9.5	336	184	81	22.8	13.6	3.41	28–16–28	1–14	14	5.01M
LONG-L2-2300-8.0	444	246	108	23.1	14.4	3.45	29–17–29	1–15	15	11.8M
WIDE-L1-2300-8.0	154	134	108	11.4	9.67	6.82	47–28–47	1–28	28	2.23M
WIDE-L2-2300-8.0	267	233	211	11.5	9.76	6.89	29–17–29	1–15	15	13.1M

TABLE 4. Mesh parameters (regions of stretching indicated with a dash).

REFERENCES

DEL ÁLAMO, J., JIMÉNEZ, J., ZANDONADE, P. & MOSER, R. D. 2004 Scaling of the energy spectra of turbulent channels. *J. Fluid Mech.* **500**, 135–144.

BANERJEE, S., KRAHL, R., DURST, F. & ZENGER, C. 2007 Presentation of anisotropy properties of turbulence, invariants versus eigenvalue approaches. *J. Turbul.* **8**, 1–27.

BLASIUS, H. 1913 Das Ähnlichkeitsgesetz bei Reibungsvorgängen in Flüssigkeiten. *Mitt. Forsch. Arb. Geb. Ing. Wes.* **131**, 1–39.

BOOKEY, P. B., WYCKHAM, C. & SMITS, A. J. 2005a Experimental investigations of Mach 3 shock-wave turbulent boundary layer interactions. In *35th AIAA Fluid Dynamics Conference and Exhibit. AIAA Paper* 2005-4899.

BOOKEY, P. B., WYCKHAM, C., SMITS, A. J. & MARTIN, M. P. 2005b New experimental data of STBLI at DNS/LES accessible Reynolds numbers. *AIAA Paper* 2005-309.

BUCKINGHAM, E. 1914 On physically similar systems: illustrations of the use of dimensional equations. *Phys. Rev.* **4**, 345–376.

CHRISTENSEN, K. T., WU, Y., ADRIAN, R. J. & LAI, W. 2004 Statistical imprints of structure in wall turbulence. In *42nd AIAA Aerospace Sciences Meeting and Exhibit. AIAA Paper* 2004-1116.

COOK, A. W. 2007 Artificial fluid properties for large-eddy simulation of compressible turbulent mixing. *Phys. Fluids* **19** (5), 055103.

DEBIEVE, J. F. & DUPONT, P. 2009 Dependence between the shock and the separation bubble in a shock wave boundary layer interaction. *Shock Waves* **19**, 499–506.

DEBONIS, J. R., OBERKAMPF, W. L., WOLF, R. T., ORKWIS, P. D., TURNER, M. G., BABINSKY, H. & BENEK, J. A. 2012 Assessment of computational fluid dynamics and experimental data for shock boundary-layer interactions. *AIAA J.* **50** (4), 891–903.

DELERY, J. & DUSSAUGE, J.-P. 2009 Some physical aspects of shock wave/boundary layer interactions. *Shock Waves* **19**, 453–468.

DOLLING, D. S. 2001 Fifty years of shock-wave/boundary-layer interaction research: what next? *AIAA J.* **39** (8), 1517–1531.

DOLLING, D. S. & MURPHY, M. T. 1983 Unsteadiness of the separation shock wave structure in a supersonic compression ramp flow field. *AIAA J.* **20** (12), 1628–1634.

DUPONT, P., HADDAD, C. & DEBIEVE, J. F. 2006 Space and time organization in a shock-induced separated boundary layer. *J. Fluid Mech.* **559**, 255–277.

DUSSAUGE, J. P., DUPONT, P. & DEBIEVE, J. F. 2006 Unsteadiness in shock wave boundary layer interactions with separation. *Aerosp. Sci. Technol.* **10**, 85–91.

FERRI, A. 1940 Experimental results with airfoils tested in the high-speed tunnel at Guidonia. NACA Tech. Rep. TM 946 (translation).

GAITONDE, D. V. & VISBAL, M. R. 1998 High-order schemes for Navier–Stokes equations: algorithm and implementation into FDL3DI. Air Force Research Laboratory Tech. Rep. AFRL-VA-WP-TR-1998-3060.

GANAPATHISUBRAMANI, B., CLEMENS, N. T. & DOLLING, D. S. 2006 Large-scale motions in a supersonic turbulent boundary layer. *J. Fluid Mech.* **556**, 271–282.

GANAPATHISUBRAMANI, B., CLEMENS, N. T. & DOLLING, D. S. 2007 Effects of upstream boundary layer on the unsteadiness of shock-induced separation. *J. Fluid Mech.* **585**, 369–394.

GANAPATHISUBRAMANI, B., CLEMENS, N. T. & DOLLING, D. S. 2009 Low-frequency dynamics of shock-induced separation in a compression ramp interaction. *J. Fluid Mech.* **636**, 497–425.

GANAPATHISUBRAMANI, B., HUTCHINS, N., HAMBLETON, W. T., LONGMIRE, E. K. & MARUSIC, I. 2005 Investigation of large-scale coherence in a turbulent boundary layer using two-point correlations. *J. Fluid Mech.* **524**, 57–80.

GARNIER, E. 2009 Stimulated detached eddy simulation of three-dimensional shock/boundary layer interaction. *Shock Waves* **19**, 479–486.

HADJADJ, A., LARSSON, J., MORGAN, B., NICHOLS, J. W. & LELE, S. K. 2010 Large-eddy simulation of shock/boundary-layer interaction. In *Center for Turbulence Research Proceedings of the Summer Program 2010*. Stanford University.

HUANG, P. G., COLEMAN, G. N. & BRADSHAW, P. 1995 Compressible turbulent channel flows: DNS results and modeling. *J. Fluid Mech.* **305**, 185–218.

HUMBLE, R. A., ELSINGA, G. E., SCARANO, F. & VAN OUDHEUSDEN, B. W. 2009*a* Three-dimensional instantaneous structure of a shock wave/turbulent boundary layer interaction. *J. Fluid Mech.* **622**, 33–62.

HUMBLE, R. A., ELSINGA, G. E., SCARANO, F. & VAN OUDHEUSDEN, B. W. 2009*b* Unsteady aspects of an incident shock wave/turbulent boundary layer interaction. *J. Fluid Mech.* **635**, 47–74.

HUMBLE, R. A., SCARANO, F. & VAN OUDHEUSDEN, B. W. 2007 Particle image velocimetry measurements of a shock wave/turbulent boundary layer interaction. *Exp. Fluids* **43**, 173–183.

HUTCHINS, N. & MARUSIC, I. 2007 Evidence of very long meandering features in the logarithmic region of turbulent boundary layers. *J. Fluid Mech.* **579**, 1–28.

IIZUKA, N. 2006 Study of Mach number effect on the dynamic stability of a blunt re-entry capsule. PhD thesis, University of Tokyo, Tokyo.

JAUNET, V., DEBIEVE, J. F. & DUPONT, P. 2012 Experimental investigation of an oblique shock reflection with separation over a heated wall. In *50th AIAA Aerospace Sciences Meeting including the New Horizons Forum and Aerospace Exposition*. AIAA Paper 2012-1095.

KAWAI, S. & LELE, S. K. 2008 Localized artificial diffusivity scheme for discontinuity capturing on curvilinear meshes. *J. Comput. Phys.* **227** (22), 9498–9526.

KAWAI, S. & LELE, S. K. 2010 Large-eddy simulation of jet mixing in supersonic crossflows. *AIAA J.* **48** (9), 2063–2083.

KAWAI, S., SHANKAR, S. K. & LELE, S. K. 2010 Assessment of localized artificial diffusivity scheme for large-eddy simulation of compressible turbulent flows. *J. Comput. Phys.* **229** (5), 1739–1762.

KNIGHT, D. D. & DEGREZ, G. 1998 Shock wave boundary layer interactions in high Mach number flows: a critical survey of current numerical prediction capabilities. *Advisory Rep.* 319. AGARD 2, 1.1–1.35.

KNIGHT, D., YAN, H., PANARAS, A. & ZHELTOVODOV, A. 2002 CFD validation for shock wave turbulent boundary layer interactions. In *40th AIAA Aerospace Sciences Meeting and Exhibit*. *AIAA Paper* 2002-0437.

KOVASZNAY, L. S. G., KIBENS, V. & BLACKWELDER, R. F. 1970 Large-scale motion in the intermittent region of a turbulent boundary layer. *J. Fluid Mech.* **41**, 283–325.

LAPSA, A. P. & DAHM, W. J. A. 2010 Stereo particle image velocimetry of nonequilibrium turbulence relaxation in a supersonic boundary layer. *Exp. Fluids* **50**, 89–108.

LAUNDER, B. E., REECE, G. J. & RODI, W. 1975 Progress in the development of a Reynolds-stress turbulence closure. *J. Fluid Mech.* **68**, 537–566.

LELE, S. K. 1992 Compact finite difference schemes with spectral-like resolution. *J. Comput. Phys.* **103** (1), 16–42.

LUMLEY, J. & NEWMAN, G. 1977 The design and application of upwind schemes on unstructured meshes. *J. Fluid Mech.* **82**, 161–178.

MANI, A., LARSSON, J. & MOIN, P. 2009 Suitability of artificial bulk viscosity for large-eddy simulation of turbulent flows with shocks. *J. Comput. Phys.* **228** (19), 7368–7374.

MORGAN, B. 2012 Large-eddy simulation of shock/turbulence interaction in hypersonic vehicle isolator systems. PhD thesis, Stanford University.

MORGAN, B., KAWAI, S. & LELE, S. K. 2011*a* A parametric investigation of oblique shockwave/turbulent boundary layer interaction using LES. In *41st AIAA Fluid Dynamics Conference and Exhibit*. *AIAA Paper* 2011-3430.

MORGAN, B., LARSSON, J., KAWAI, S. & LELE, S. K. 2011*b* Improving low-frequency characteristics of recycling/rescaling inflow turbulence generation. *AIAA J.* **49** (3), 582–597.

MORGAN, B. & LELE, S. K. 2011 Turbulence budgets in oblique shockwave/turbulent boundary layer interactions. In *Center for Turbulence Research Annual Research Briefs*, pp. 75–86. Stanford University.

MORRISON, J. H. 1992 A compressible Navier–Stokes solver with two-equation and Reynolds stress turbulence closure models. NASA Tech. Rep. CR-4440.

OBAYASHI, S., FUJI, K. & GAVALI, S. 1988 Navier–Stokes simulation of wind-tunnel flow using LU-ADI factorization algorithm. NASA Tech. Rep. TM-100042.

PECNIK, R., TERRAPON, V. E., HAM, F. & IACCARINO, G. 2009 Full system scramjet simulation. In *Center for Turbulence Research Annual Briefs*. Stanford University.

PIPONNIAU, S., DUSSAUGE, J. P., DEBIEVE, J. F. & DUPONT, P. 2009 A simple model for low-frequency unsteadiness in shock-induced separation. *J. Fluid Mech.* **629**, 87–108.

PIROZZOLI, S., BEER, A., BERNARDINI, M. & GRASSO, F. 2009 Computational analysis of impinging shock-wave boundary layer interaction under conditions of incipient separation. *Shock Waves* **19**, 487–497.

PIROZZOLI, S. & BERNARDINI, M. 2011 Direct numerical simulation database for impinging shock wave/turbulent boundary-layer interaction. *AIAA J.* **49** (6), 1307–1312.

PIROZZOLI, S. & GRASSO, F. 2006 Direct numerical simulation of impinging shock wave/turbulent boundary layer interaction at $M = 2.25$. *Phys. Fluids* **18**, 065113.

PIROZZOLI, S., GRASSO, F. & GATSKI, T. B. 2004 Direct numerical simulation and analysis of a spatially evolving supersonic turbulent boundary layer at $M = 2.25$. *Phys. Fluids* **16** (3), 530–545.

PIROZZOLI, S., LARSSON, J., NICHOLS, J. W., BERNARDINI, M., MORGAN, B. & LELE, S. K. 2010 Analysis of unsteady effects in shock/boundary layer interactions. In *Center for Turbulence Research Proceedings of the Summer Program 2010*. Stanford University.

PLOTKIN, K. J. 1975 Shock wave oscillation driven by turbulent boundary-layer fluctuations. *AIAA J.* **13** (8), 1036–1040.

POGGIE, J. & SMITS, A. J. 2005 Experimental evidence for Plotkin model of shock unsteadiness in separated flow. *Phys. Fluids* **17**, 018107.

ROBINET, J.-CH. 2007 Bifurcations in shock-wave/laminar-boundary-layer interaction: global instability approach. *J. Fluid Mech.* **579**, 85–112.

SMITS, A. J. & DUSSAUGE, J.-P. 2006 *Turbulent Shear Layers in Supersonic Flow*. Springer.

SMITS, A. J., MCKEON, B. J. & MARUSIC, I. 2011 High-Reynolds number wall turbulence. *Annu. Rev. Fluid Mech.* **43**, 353–375.

SOUVEREIN, L. J. 2010 On the scaling and unsteadiness of shock induced separation. PhD thesis, Université de Provence Aix–Marseille I.

SPALART, P. R. & ALLMARAS, S. R. 1994 A one-equation turbulence model for aero-dynamic flows. *Rech. Aerosp.* **1**, 5–21.

STEWARTSON, K. 1974 Multistructured boundary layers on flat plates and related bodies. *Adv. Appl. Mech.* **14**, 145–239.

TOUBER, E. & SANDHAM, N. D. 2008 Oblique shock impinging on a turbulent boundary layer: low-frequency mechanisms. In *38th AIAA Fluid Dynamics Conference and Exhibit. AIAA Paper* 2008-4170.

TOUBER, E. & SANDHAM, N. D. 2009*a* Comparison of three large-eddy simulations of shock-induced turbulent separation bubbles. *Shock Waves* **19**, 469–478.

TOUBER, E. & SANDHAM, N. D. 2009*b* Large-eddy simulation of low-frequency unsteadiness in a turbulent shock-induced separation bubble. *Theor. Comput. Fluid Dyn.* **23**, 73–107.

TOUBER, E. & SANDHAM, N. D. 2011 Low-order stochastic modeling of low-frequency motions in reflected shock-wave/boundary-layer interactions. *J. Fluid Mech.* **671**, 417–465.

URBIN, G. & KNIGHT, D. 2001 Large-eddy simulation of a supersonic boundary layer using an unstructured grid. *AIAA J.* **39** (7), 1288–1295.

WILCOX, D. C. 2006 *Turbulence Modeling for CFD*, 3rd edn. DCW Industries, Inc.